Palaeogeography, Palaeoclimatology, Palaeoecology 538 (2020) 109423

Contents lists available at ScienceDirect

Palaeogeography, Palaeoclimatology, Palaeoecology

journal homepage: www.elsevier.com/locate/palaeo

A Mississippian black shale record of redox oscillation in the Craven Basin, UK

Joseph F. Emmings[a,b,*], Simon W. Poulton[c], Christopher H. Vane[a], Sarah J. Davies[b], Gawen R.T. Jenkin[b], Michael H. Stephenson[a], Melanie J. Leng[a,d], Angela L. Lamb[a], Vicky Moss-Hayes[a]

[a] British Geological Survey, Keyworth, Nottingham, NG12 5GG, UK
[b] School of Geography, Geology and the Environment, University of Leicester, Leicester, LE1 7RH, UK
[c] School of Earth and Environment, University of Leeds, Leeds, LS2 9JT, UK
[d] Centre for Environmental Geochemistry, Sutton Bonington Campus, University of Nottingham, Sutton Bonington, Leicestershire, LE12 5RD, UK

ARTICLE INFO

Keywords:
Palaeoredox
Diagenesis
Epicontinental
Bowland shale

ABSTRACT

Early diagenetic redox oscillation processes have been rarely recognised in the ancient rock record but potentially exert an important control on mineral authigenesis, hydrocarbon prospectivity and supply of metals and/or reduced S as part of associated mineral systems. The upper unit of the Mississippian Bowland Shale Formation is a candidate record of diagenetic redox oscillation processes because it was deposited under a relatively high sediment accumulation rate linked to a large delta system, and under dominantly anoxic and intermittently sulphidic bottom-water conditions. In order to characterise the syngenetic and early diagenetic processes, sedimentological and geochemical data were integrated through the Upper Bowland Shale at three sites in the Craven Basin (Lancashire, UK). Organic matter (OM) comprises a mixture of Type II, II-S, II/III and III OM. 'Redox zones' are defined by patterns of Fe-speciation and redox-sensitive trace element enrichment and split into two groups. 'Sulphidic' zones (EUX, AN-III, AN-I and AN-IT) represent sediments deposited under conditions of at least intermittently active sulphate-reduction in bottom-waters. 'Non-sulphidic' zones (OX-RX, OX-F and OX) represent sediments deposited under non-sulphidic (oxic to ferruginous anoxic) bottom-waters. Operation of a shelf-to-basin 'reactive Fe' (Fe_{HR}) shuttle, moderated by sea level fluctuation and delta proximity, controlled the position and stability of redoxclines between zones of Fe and sulphate reduction, and methanogenesis. Early diagenetic redoxclines were capable of migration through the shallow sediment column relatively quickly, in response to sea level fluctuation. Preservation of syngenetic and early diagenetic geochemical signals shows redoxclines between Fe and sulphate reduction, and the upper boundary of sulphate-methane transition zone, were positioned within decimetres (i.e., 10 s cm) of seabed. Falling sea level and increasing Fe_{HR} supply is recognised as a switch from zones EUX (high sea level), AN-III and ultimately AN-I and AN-IT (low sea level). Zone AN-I defines the operation of 'redox oscillation', between zones of Fe and sulphate reduction in shallow porewaters, associated with enhanced degradation of OM and complete dissolution of primary carbonate. Preservation of OM and carbonate, in this system, was a function of changing bottom and pore water redox processes. Redox oscillation operated in a siliciclastic, prodeltaic environment associated with a relatively high sediment accumulation rate and high loadings of labile organic matter and metal oxides. These findings are important for understanding Late Palaeozoic black shales in the context of hydrocarbon and mineral systems.

1. Introduction

Organic-rich marine sediments subject to intense physical reworking and in receipt of a large supply of metal oxidants, such as in the modern Amazon fan, are prone to early diagenetic 'redox oscillation' (Aller, 1998; Aller and Rude, 1988; Michalopoulos and Aller, 2004). Redox oscillation describes the vertical migration of redoxclines bounding zones in the shallow sedimentary column (e.g., Burdige, 2006), where O_2, NO_3^- (nitrate), Mn^{4+}, Fe^{3+} and/or SO_4^{2-} (sulphate) may be the dominant terminal electron acceptors (Froelich et al., 1979), and/or the zone where methanogenesis dominates (Claypool and Kaplan, 1974). Redox oscillation greatly enhances the rate of organic

---

* Corresponding author. British Geological Survey, Keyworth, Nottingham, NG12 5GG, UK.
E-mail address: josmin65@bgs.ac.uk (J.F. Emmings).

https://doi.org/10.1016/j.palaeo.2019.109423
Received 14 August 2019; Received in revised form 22 October 2019; Accepted 23 October 2019
Available online 05 November 2019

matter (OM) remineralisation in marine sediments (Aller, 1994, 1998; Burdige, 2007; Sun et al., 2002) by increasing the exposure time to oxidants yielding the highest free energy, particularly oxygen (Hartnett et al., 1998).

In oxygen-deficient conditions, bacterial metabolism dominates OM remineralisation, first utilizing NO_3^- (denitrification), followed by Mn^{4+}, Fe^{3+}, sulphate, and ultimately CO_2. Methanogens, utilizing acetate and CO_2 as the two major substrates, are usually out-competed by sulphate-reducers in shallow marine sediments (Jorgensen, 1982). Suboxic to anoxic, low pressure and temperature seabed conditions also support abiotic reduction of NO_3^- and metal oxides (Mn^{4+}, Fe^{3+}, e.g., Burdige, 2006). This dual operation of biological and abiotic NO_3^- and metal oxide reduction pathways at typical seabed conditions compresses the zones of denitrification and Mn/Fe reduction in near-surface sediments (Burdige, 2006). These processes typically ensure, under anoxic marine conditions, dominance of sulphate reduction in shallow porewaters (Thamdrup, 2000).

Under oxic bottom-water conditions, redox oscillation is stimulated by bottom-currents and bioturbation, which enhance physical reworking and increase exposure to O_2 in shallow sediments (Aller, 1994). Aerobic bacteria, coupled to the use of O_2 by enzyme cofactors, are capable of degrading a wide range of complex organic compounds (e.g., Fenchel et al., 2012) and remineralisation of OM via hydrolysis and/or oxidative cleavage. Under more oxygen-limited conditions, bottom-current reworking and metal oxide loading also stimulate redox oscillation processes, typically between zones of Mn^{4+}, Fe^{3+} and sulphate reduction (Aller, 1998). Metal oxide reduction (Thamdrup, 2000) and co-oxidation processes (Aller, 1994; Bianchi, 2011; Canfield, 1994) enhance OM remineralisation under these conditions.

As a consequence of these processes, rapid and permanent OM burial beneath the sulphate-methane transition zone (e.g., Claypool and Kaplan, 1974; Scotchman, 1989; Krajewski et al., 2001; Malinverno and Pohlman, 2011) will promote OM preservation. This likely proceeds via 'selective preservation' (Tegelaar et al., 1989) of non-hydrolisable biopolymers (Henrichs, 1992), accumulation of bacterial 'biomass' (Gong and Hollander, 1997) perhaps protected by authigenic or detrital minerals (Bennett et al., 1999; Keil and Mayer, 2014; Mayer, 1994), 'classical' geopolymerisation reactions (Nissenbaum and Kaplan, 1972), and/or cross-linking by heteroatoms such as S (Sinninghe Damsté et al., 1987; Tegelaar et al., 1989) and N (Knicker, 2004). This complexity of early diagenetic processes combined with other factors, such as productivity, explains why the oxygen content of bottom-waters is not necessarily correlated with an improved hydrocarbon source rock potential (Ganeshram et al., 1999).

Early diagenetic redox oscillation processes have been rarely studied or recognised in the ancient rock record (e.g., Lash, 2015), but potentially exert an important control on mineral authigenesis (Curtis, 1977), hydrocarbon prospectivity (Espitalie et al., 1977) and supply of metals and/or reduced S, with relevance, for example, in carbonate-hosted Zn–Pb mineral systems (e.g., Ashton et al., 2016). The record of redox oscillation is particularly likely in siliciclastic, prodeltaic and deltaic mudstones associated with relatively high mean sediment accumulation rates and high loadings of both OM and metal oxides. The upper unit of the Mississippian Bowland Shale Formation is a candidate record of diagenetic redox oscillation processes, because it was; deposited under a relatively high mean sediment accumulation rate as part of a remotely linked delta system (Emmings et al., 2019a), and; deposited under dominantly anoxic and intermittently sulphidic bottom-water conditions (Emmings et al., 2019b). The Upper Bowland Shale is a prodeltaic succession, recognised for significant spatial and temporal compositional heterogeneity driven by fourth-order sea level cyclicity (e.g., Clarke et al., 2018; Emmings et al., 2019a; Waters et al., 2019). The Bowland Shale and equivalents are the targets for unconventional hydrocarbon exploration in the UK (Andrews, 2013; Clarke et al., 2018; Waters et al., 2019).

In order to address the role of redox oscillation processes, sedimentological observations, organic and inorganic geochemistry and stable isotopes were integrated from three sections of the Upper Bowland Shale in the Craven Basin (Lancashire, UK). We expand on the model for anoxia proposed by Emmings et al. (2019b), who related the distribution of palynofacies and organic sulphur to changing syngenetic and early diagenetic redox conditions in the Bowland Shale. Here we explore a wider geochemical dataset which shows the state and stability of bottom-water and pore-water redoxclines exerted a key control on the type and distribution of OM, diagenetic mineral suites and metals through this black shale succession.

2. Geological setting

The Bowland Shale Formation was deposited in a series of epicontinental basins as part of the Rheic-palaeo-Tethys palaeoequatorial seaway spanning from present-day North America to Poland (e.g., Davydov et al., 2012). This seaway developed in response to oblique collision between Gondwana and Laurussia (Warr, 2000), including phases of rifting, thermal subsidence, strike-slip and compression tectonism. Mississippian extension (Leeder, 1982) generated a series of graben and half-graben structures, separated by platform 'blocks' and 'highs', referred to as a 'block-and-basin' topography (Fig. 1a; e.g., Waters and Davies, 2006). Transition from active rifting to thermal subsidence broadly coincides with subdivision of the Bowland Shale Formation into lower and upper units at the Visean-Serpukhovian boundary (Bisat, 1923; Davydov et al., 2012; Earp, 1961; Menning et al., 2006; Waters et al., 2009). The Upper Bowland Shale was deposited from the early to late Pendleian (~330–329.7 Ma; Gastaldo et al., 2009; Waters and Condon, 2012) in the Craven Basin (Fig. 1d).

The switch from rift to thermal sag, coupled with the advance of Pendle fluviodeltaic systems from the north (Fig. 1a; e.g., Waters et al., 2014; Bijkerk, 2014), produced an interdigitating succession of hemipelagic and siliciclastic facies in the Craven Basin (Fig. 1d). The Upper Bowland Shale was deposited relatively rapidly (Fig. 1b), defining a key prodeltaic transition between the carbonate-dominated Lower Bowland Shale (Newport et al., 2018) and the overlying siliciclastic, deltaic Millstone Grit Group (including the Pendleton Formation; Fig. 1; Waters et al., 2009).

Emmings et al. (2019a) interpreted 'lenticular' mudstones, common in the Upper Bowland Shale, primarily as 'densite' mud mixed with subordinate hemipelagic mud. This texture is best explained by the transport and deposition of mud rip-up intraclasts in the bedload of density currents (see Schieber et al., 2010) that is mixed with hemipelagic and turbiditic mud. Mud intraclasts were likely sourced from nearby highs and blocks proximal to the Pendle delta, suggesting the Upper Bowland Shale was 'remotely linked' to the prograding Pendle delta system (Emmings et al., 2019a).

Siliciclastic facies also include a variety of turbidites, hybrid beds, debrites and the partially injected Hind Sandstone Member (Aitkenhead et al., 1992; Emmings et al., 2019a; Kane, 2010; Moseley, 1952, 1962). Deposition of the Bowland Shale was followed by deposition of delta-top facies on the Askrigg Block and the Pendle Grit basinal submarine turbidite fan complex as part of the Pendleton Formation (Fraser and Gawthorpe, 1990, 2003; Kirby et al., 2000; Waters et al., 2007, 2009) (Fig. 1d). Estimates for water depth in the Craven Basin range from ~100 to 200 m (Davies, 2008; Holdsworth and Collinson, 1988), to several hundred metres (Davies et al., 1993).

2.1. Condensed sections

Hemipelagic sediments in the Bowland Shale include discrete, macrofauna-bearing, commonly carbonate-rich sedimentary packages termed 'marine bands' (e.g., Ramsbottom, 1977, Fig. 1d). Marine bands are interpreted as 'condensed sections'; sediments starved of terrigenous material deposited during periods of the maximum rate of transgression (Posamentier et al., 1988) and/or at maximum marine

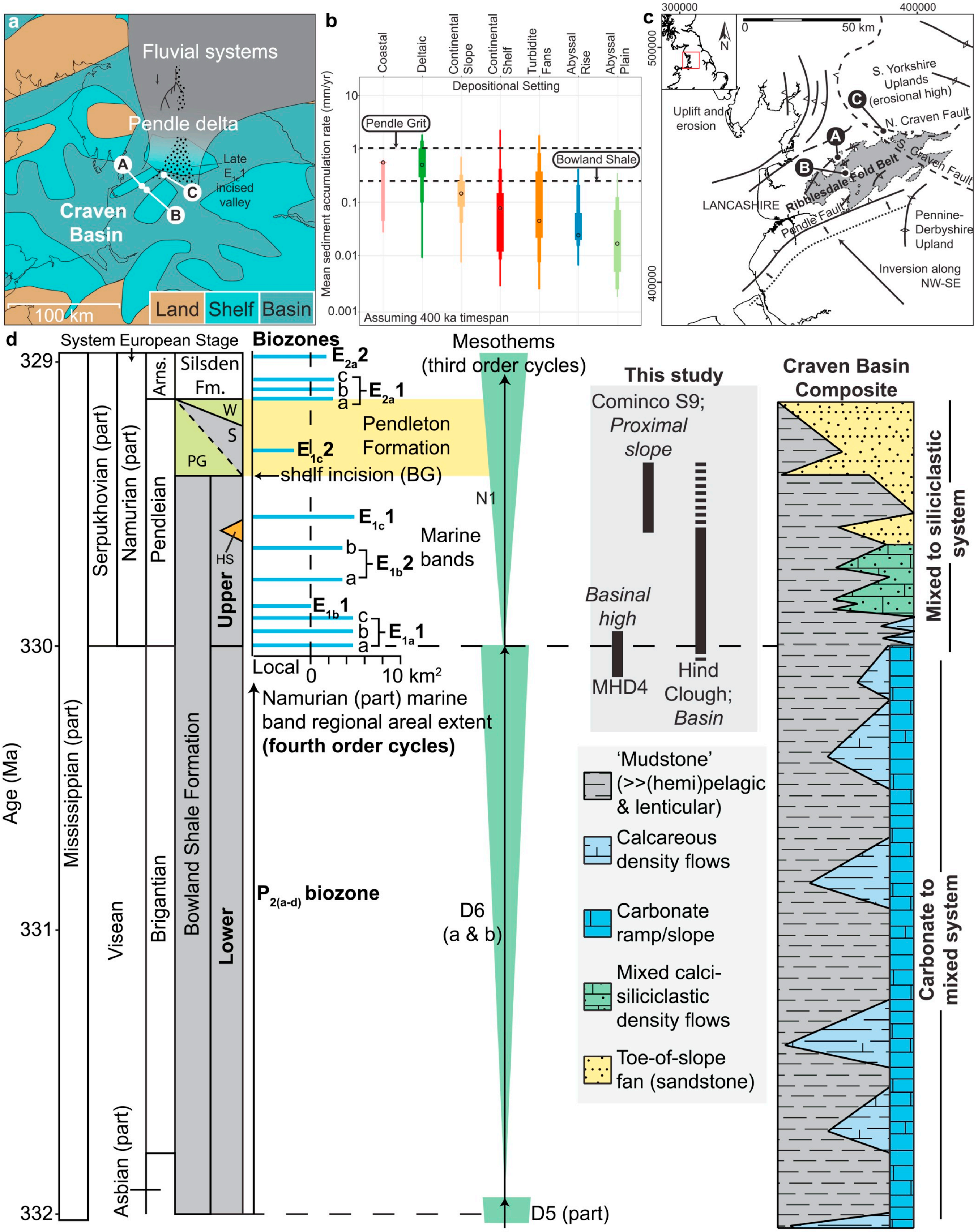

(caption on next page)

Fig. 1. a) Inherited Visean regional basin structure, modified from Waters et al. (2007). Hind Clough (A), MHD4 (B) and Cominco S9 (C). Pendle delta and feeder system extent based on Fraser and Gawthorpe (1990, 2003), Waters et al. (2014) and Bijkerk (2014) and references therein. Late $E_{1c}1$ incised valley (Bearing Grit) extent from Bijkerk (2014). Major Pendleian fluvial systems, including the compound fill of the Rogerley Channel, from Waters et al. (2014). b) Mean sediment accumulation rate (SAR) versus time span for siliciclastic sedimentary systems after Sadler (1981, 1999) and Sadler and Jerolmack (2014), assuming 400 ka timespan of deposition. Plotted with median values and 1σ (thick), 2σ (medium) and 3σ (thin) percentiles. c) Location map with main structural elements (after Fraser and Gawthorpe, 2003) Hind Clough (A), MHD4 (B) and Cominco S9 (C). Outcrop extent data based on DigMapGB-625, with permission of the British Geological Survey. British National Grid projection. Contains Ordnance Survey data © Crown Copyright and database rights. d) Generalised Visean-Serpukhovian lithochronostratigraphy, including the Upper Bowland Shale (this study) and Hind Sandstone Member (HS), from Emmings et al. (2019a). Age control from Waters and Condon (2012) after Gastaldo et al. (2009) and Davydov et al. (2010). Estimated areal extent for marine bands from Waters and Condon (2012). Diagnostic ammonoid faunal zones from Riley et al. (1993) and mesothem definitions from Ramsbottom (1973, 1977). Craven Basin composite after Newport et al. (2018) and Brandon et al. (1998). The Pendleton Formation includes the Pendle Grit Member (PG), Surgill Shale (S), Warley Wise Grit (W) and Bearing Grit incised valley infill (BG).

flooding (Martinsen et al., 1995). Marine band cyclicity in the Namurian was likely a response to far-field ice-sheet volume on Gondwana (Veevers and Powell, 1987).

Marine bands typically include thick- and thin-shelled body fossils hosted within a weakly to moderately lenticular, typically carbonate-rich, mud-rich matrix (Emmings et al., 2019a). Macrofaunal body fossils, particularly ammonoids, are used to differentiate marine bands from intervening mudstones and permit a high-resolution biostratigraphic framework (Ramsbottom and Saunders, 1985). The Upper Bowland Shale in the study area contains four index marine bands, $E_{1a}1$ to $E_{1c}1$, which correspond to the base of four ammonoid (sub)zones, *Cravenoceras leion, Cravenoceras bradoni, Tumulites pseudobilinguis* and *Cravenoceras malhamense*, respectively (e.g., Brandon et al., 1998). The $E_{1a}1$ marine band is an important marker package at the Lower-Upper Bowland Shale contact (Fig. 1d). Marine bands and overlying mudstones may exhibit a complete faunal succession (phases 6 to 1); thick shelled goniatites (6), thin shelled goniatites (5), molluscan spat (4), *lingula* (3), *planolites* (2), fish remains (1), as well as barren zones (Ramsbottom, 1977). These faunal phases are thought to indicate cycling between euhaline (6) and freshwater conditions (1) (Holdsworth and Collinson, 1988; Ramsbottom et al., 1962).

Marine bands are interpreted as fourth-order sequences (Mitchum and Van Wagoner, 1991). $E_{1a}1$ and $E_{1c}1$, thought to represent peak highs associated with the ~400 ka eccentricity cycle (Maynard and Leeder, 1992; Waters and Condon, 2012). Multiple flooding surfaces are recognised for $E_{1a}1$ (a, b and c) and $E_{1b}2$ (a and b) marine bands (Waters and Condon, 2012), which may represent higher-frequency sea level fluctuations (Fig. 1d). Estimates for the amplitude of sea level cycles ranges between 42 m (Maynard and Leeder, 1992) to 60–100 m (Church and Gawthorpe, 1994; Rygel et al., 2008). The Upper Bowland Shale and overlying Pendleton Formation form part of the N1 mesothem (Ramsbottom, 1973, 1977), a candidate third-order sequence (Mitchum and Van Wagoner, 1991, Fig. 1d).

Variscan inversion of the Craven Basin, primarily during the Pennsylvanian (Late Westphalian to Stephanian; e.g., Pharaoh et al., 2019), resulted in the development of a set of north-east south-west trending folds, thrust-folds and monoclines. These structures are collectively defined as the Ribblesdale Fold Belt (Arthurton, 1984; Gawthorpe, 1987, Fig. 1c).

3. Materials and methods

Three localities in the Craven Basin were selected for geochemical analysis; the outcrop at Hind Clough (53°58′25.4″N 2°32′37.6″W, WGS1984) and boreholes Marl Hill 4 (MHD4; 53° 54′ 57.17″N 2° 29′ 50.68″W) and Cominco S9 (54° 4′ 2.08″N 2° 12′ 54.93″W; Fig. 1c). The stratigraphic framework for these sections was based on ammonoid biozones $P_{2c\text{-}d}$ to $E_{1c}1$ (see geological setting) identified by Brandon et al. (1998), Riley (1988) and Arthurton (1972), respectively. Sedimentary facies descriptions and bioturbation index (BI) are based on the method of Lazar et al. (2015). BI is defined on a scale of increasing bioturbation intensity, where 0 indicates the sample is not bioturbated and 5 indicates complete churning by infauna.

3.1. *Rock-Eval pyrolysis and n-alkanes*

Subsamples were crushed and milled to a fine powder prior to geochemical analysis. Pyrolysis was conducted on 193 whole-rock bulk powders in a Rock-Eval 6™ apparatus (Vinci Technologies) in standard mode. This included pyrolysis of 8 samples following extraction of bitumen (Soxhlet extraction; Appendix A). Gas chromatography (GC) analyses were conducted on *n*-alkane extracts from 30 immature to early oil-mature samples from Hind Clough and MHD4. Powders (10 g) were spiked with tetracosane-D50, squalene and hexatriacontane-D74 at 10 ng/μL and allowed to equilibrate for 3 h. Powders were then mixed with clean sand (43 g) and copper powder (6 g), prior to extraction with dichloromethane (DCM)/methanol (9:1 v/v) at 75 °C and 750 psi using an accelerated solvent extraction system (ASE, Dionex 200; e.g., Newell et al., 2016). Extracts were reduced to dryness using a TurboVap and reconstituted in a minimum volume of DCM for column chromatography. Saturated hydrocarbons were separated using a glass pipette alumina oxide column (Al_2O_3-5x0.5 cm) eluted with 4 ml *n*-hexane/DCM (9:1 v:v) then reconstituted in 0.5 mL volume of n-hexane for GC analysis.

Saturates were analysed on a Hewlett Packard 6890 series GC-FID system fitted with an Agilent J&W DB-1 column (60 m length, 0.25 mm internal diameter, 0.1 μm film thickness), 1 μL was injected at 280 °C in splitless mode for 0.7 min, split 1:30 thereafter. Helium carrier gas was supplied at 1 mL/min. The oven temperature program ramped from 60 °C (isothermal for 1 min) to 320 °C (isothermal for 15 min) at 10 °C/min. Peak area integrations were determined using Clarity software. Extracts included identification of isoprenoids pristane (Pr) and phytane (Ph). The terrigenous/aquatic *n*-alkane ratio (TAR; Eq. (1)) was used to assess the relative contributions of terrestrial and marine OM (Bourbonniere and Meyers, 1996). Data and chromatograms are presented in Appendix B.

$$\text{TAR} = (nC_{27} + nC_{28} + nC_{29})/(nC_{15} + nC_{17} + nC_{19}) \tag{1}$$

3.2. *Major and trace elements*

Total carbon (C) and sulphur (S) concentrations were measured on 110 samples using a LECO CS 230 elemental analyser. Major and trace element concentrations were measured on fused beads (109 samples) and powder briquettes (108 samples) with a PANalytical Axios Advanced X-Ray Fluorescence (XRF) spectrometer using default PANalytical SuperQ conditions. Data, including estimates for accuracy and precision, are reported in Appendix C. Trace element enrichment factors (EFs; e.g., Tribovillard et al., 2006) were utilised (Eq. (2)), using Post-Archaean Average Shale (PAAS) (Taylor and McLennan, 1985). As, Sb and Se were normalised to Upper Continental Crust (McLennan, 2001) in the absence of PAAS values. 'Excess Si' was calculated (Emmings et al., 2019a) using Si/Al ≤ 2.5 as the local detrital signal (*sensu* Sholkovitz and Price, 1980, Eq. (3)) and interpreted primarily as a pelagic and biogenic (radiolarian) signal that did not migrate significantly during diagenesis (Emmings et al., 2019a). Fe_T, S, Mo and U data were previously reported by Emmings et al. (2019b).

$$EF_{element} = [X/Al]_{sample}/[X/Al]_{PAAS} \quad (2)$$

$$Si_{excess} = Si - (2.5xAl) \quad (3)$$

3.3. Iron speciation

Fe speciation analyses were reported by Emmings et al. (2019b), and were conducted via sequential extraction to determine carbonate-associated Fe (Fe_{carb}), ferric (oxyhydr)oxides (Fe_{ox}) and magnetite (Fe_{mag}) (Poulton and Canfield, 2005). Fe-speciation data plotted versus depth are provided in Appendix D. The precision of Fe_{ox}, Fe_{mag} and Fe_{ox} was determined as < ± 0.01 wt%, based on two standard deviations (2σ) of repeat analyses. Pyrite Fe (Fe_{py}) was estimated via extraction of chromium-reducible S, which followed extraction of acid-volatile sulphide (Canfield et al., 1986). The precision of Fe_{py} was determined as ± 0.11 wt%. The sum of Fe_{carb} + Fe_{ox} + Fe_{mag} + Fe_{py} defines a 'highly reactive' (Fe_{HR}) pool (Poulton et al., 2004a), consisting of Fe mineral phases considered to be reactive towards dissolved sulphide (Canfield et al., 1992; Poulton et al., 2004b). Fe_{HR}/Fe_T (total Fe) and Fe_{py}/Fe_{HR} were compared with established redox thresholds (Poulton and Canfield, 2011; Poulton and Raiswell, 2002; Raiswell and Canfield, 1998). Facies H–I Fe_{HR} is presented on a Fe_{mag}-free basis, due to the presence of detrital Fe_{mag} (i.e., Facies H–I are compositionally immature; see Emmings, 2018; Emmings et al., 2019a).

3.4. Organic sulphur

Organic S (S_{org}) data were previously reported by Emmings et al. (2019b). 37 sample powders (~1 g) were washed for 24 h in 200 ml 10 wt/vol % NaCl in order to leach free sulphate (Kampschulte et al., 2001). Total S measured on NaCl-washed residues was compared with the total S of untreated powders, yielding an estimate for the sulphate S (S_{sul}) fraction, after correction for the mass loss assuming leaching of pure $CaSO_4$ (see Emmings et al., 2019b). In most cases, estimated S_{sul} was within or close to ± 0.08 wt % (2σ) of the total (untreated) S (i.e., the long-term analytical precision). Therefore S_{sul} was negligible for most samples. S_{org} content was estimated by subtraction of S_{py} (Fe_{py} x 1.15) and S_{sul} from total S (Eq. (4); e.g., Tribovillard et al., 2001). Propagating the precision of TS, S_{py} and S_{sul} in quadrature yields a precision estimate of ± 0.12 wt % (2σ) for S_{org}.

$$S_{org} = S - S_{py} - S_{sul} \quad (4)$$

3.5. Stable isotopes

All stable isotope data are reported in standard delta (δ) notation as per mille (‰) variations. Stable C isotope analyses of OM ($\delta^{13}C_{org}$) were determined on decarbonated powders by combustion in a Costech ECS4010 elemental analyser and GV Optima isotope ratio mass spectrometer. Reported $\delta^{13}C_{org}$ values are reported on the Vienna Pee Dee Belemnite (VPDB) scale, using a within-run laboratory standard, BROC2 (−27.5‰), which is calibrated against international standards NBS19 (+1.95‰) and NBS22 (−30.03‰). $\delta^{13}C_{org}$ reproducibility is ± 0.1‰ (2σ). S isotope ratios for chromium-reducible (pyrite S) extracts (as Ag_2S) were measured using a Thermo Delta Plus XL isotope ratio mass spectrometer interfaced with a Flash 1112 elemental analyser. $\delta^{34}S_{py}$ values are reported on the VCDT scale. $\delta^{34}S_{py}$ data are reported in Emmings et al. (2019b) and Table 1. S isotope ratios were calibrated using a linear two-point fit through IAEA-S-1 (−0.3‰) and IAEA-S-3 (−32.3‰). IAEA-S-2 (+22.67‰) was also analysed as an unknown. $\delta^{34}S_{py}$ reproducibility is ± 1.0‰ (2σ) based on repeat analyses.

The C and O stable isotope composition of carbonate ($\delta^{13}C_{carb}$ and $\delta^{18}O_{carb}$) was measured on a VG Optima dual inlet mass spectrometer using samples pre-treated with 5% sodium hypochlorite to oxidise reactive organic material. Prior to analysis the samples were reacted overnight in vacuo with anhydrous phosphoric acid at 25 °C, and the liberated CO_2 was separated cryogenically from water vapour under vacuum. $\delta^{13}C_{carb}$ and $\delta^{18}O_{carb}$ values are reported on the VPDB scale using a within-run laboratory standard, MCS (−0.95‰ $\delta^{13}C$, −9.17‰ $\delta^{18}O$), calibrated against international standards NBS19 (+1.95‰ $\delta^{13}C$, −2.20‰ $\delta^{18}O$) and NBS18 (−5.01‰ $\delta^{13}C$, −23.2‰ $\delta^{18}O$). Repeat analyses indicate reproducibility of ± 0.12‰ (2σ) and ± 0.02‰ (2σ), for $\delta^{13}C_{carb}$ and $\delta^{18}O_{carb}$, respectively. Selected $\delta^{13}C_{org}$, $\delta^{13}C_{carb}$ and $\delta^{18}O_{carb}$ isotopic data are reported in Appendix E. All data are available in the accompanying supplementary files and stored in an open-access data repository (Emmings et al., 2019c). All data (with the exception of $\delta^{13}C_{carb}$ and $\delta^{18}O_{carb}$) were first reported in Emmings (2018) [PhD thesis under embargo until late 2020].

4. Results

Sections were logged and sampled. Sedimentary facies A-J were defined and interpreted by Emmings et al. (2019a). Facies A are thin-bedded spherulitic limestones present at the base of the $E_{1a}1$ marine band. Facies B–C are siliceous, calcareous, bioclastic (B) to non-bioclastic (C) lenticular argillaceous mudstones deposited dominantly under hemipelagic conditions during periods of high sea level ('marine band' packages). Facies D-E are siliceous, calcareous, argillaceous mudstones interpreted as a variety of density flow deposits including calciturbidites (D) and silici-turbidites, debrites and hybrid flows (E) deposited during falling and low sea level. Facies Em represent the 'mud cap' equivalent of Facies E hybrid beds. Facies F are siliceous lenticular argillaceous mudstones deposited under hemipelagic conditions with enhanced bedload transport of mud clasts during periods of falling sea level.

Facies G are argillaceous, strongly lenticular mudstones that lack quartz and carbonate cement. Organic-rich laminae in Facies G were interpreted by Emmings et al. (2019a) and Emmings et al. (2019b) as the fragments of sulphide-oxidising microbial mats. Facies H-J are a variety of siliciclastic sediments, including argillaceous mudstones (H), siltstones (I) and rare sandstones (J), deposited primarily from density flows. Facies G-J were deposited during the late stages of basin infill as part of the Pendle prodelta, prior to deposition of the Pendleton Formation (Emmings et al., 2019a). Sedimentary logs and selected data from Hind Clough, MHD4 and Cominco S9 are presented in Figs. 2–3 and Tables 1–4.

4.1. Organic geochemistry

Plotting T_{max} versus hydrogen index (HI) demonstrates that samples from Hind Clough and MHD4 are immature to early oil mature, whereas most Cominco S9 samples are oil mature (Fig. 4a). TOC and HI are typically highest in Facies A-F, and A-C (i.e., marine bands), respectively (Figs. 2–3, 4a-c, Table 1). A pseudo-van krevelen plot (e.g., Espitalie et al., 1977; Peters, 1986, Fig. 4b) demonstrates samples from Hind Clough and MHD4 plot closest to the Type I maturation pathway. Facies D-E and H–I are positioned near the Type III pathway. OI is low in Facies A-C (marine bands) and F-G, and highly variable in Facies D-E and H–I. Plotting S2 versus TOC demonstrates that most samples plot within the mixed Type II/III to Type III OM fields (Fig. 4c). Facies A-C and F are differentiated along HI = 200 mg HC/g TOC_{pd} (Fig. 4c) and the ratio of pyrolised to residual organic C (PC/RC = 0.2; Fig. 4d). Facies D and E plot along PC/RC = 0.2. Facies A-C and Em-I mudstones plot above, and below, this line, respectively. The $E_{1c}1$ marine band at Cominco S9 exhibits decreased T_{max} compared to adjacent Facies H–I mudstones above and below (Fig. 2). At Hind Clough and MHD4, T_{max} is lowest in Facies F (~433 °C) and highest in Facies B and G (~440 °C; Table 1; Fig. 3).

Extracted *n*-alkanes are generally dominated by relatively short chains (Fig. 4e) and exhibit an average ACL of ~18.7 and TAR of 0.10

Table 1

Selected parameters for coupled Rock-Eval pyrolysis, Fe speciation, trace element and S isotope analyses.

Sample	Location	Depth/ Height [m]	Facies	T_{max} [°C]	PC [%]	RC [%]	TOC [%]	HI [mgHC/ gTOC]	pyro MINC [%]	oxi MINC [%]	Fe_{HR}/Fe_{T}*	Fe_{py}/Fe_{HR}*	Ni [EF]	V [EF]	V/(V + Ni) [EF]	S_{py} [%]	S_{sul} [%]	S_{org} [%]	Atomic S/C_{org}	$\delta^{34}S_{py}$ [‰]
SSK60768	MHD4	10.80	A	435	0.72	1.94	2.66	281	0.38	6.39	0.82	0.51	2.48	8.71	0.78	0.91	0.12	0.01	0.00	−29.32
HC02_20	HC	21.80	A	439	0.17	0.95	1.12	138	0.56	8.86	0.92	0.26	2.12	7.88	0.79	1.05	0.06	< LLD	–	−16.51
HC02_2	HC	0.68	B	442	0.76	2.67	3.43	218	0.25	2.84	0.96	0.77	2.90	8.42	0.74	1.75	0.13	0.21	0.02	−30.82
HC02_13	HC	11.60	B	442	0.65	2.66	3.31	203	0.20	1.82	1.00	0.76	2.84	7.33	0.72	1.48	0.16	0.13	0.01	−30.05
HC02_14	HC	12.90	B	435	1.43	3.44	4.87	319	0.28	3.37	0.86	0.61	3.45	9.56	0.73	1.56	0.06	0.13	0.02	−33.00
SSK60774	MHD4	12.90	B	441	0.52	2.43	2.95	173	0.44	5.07	1.00	0.80	3.24	9.79	0.75	1.87	0.14	0.14	0.01	−32.10
HC02_16	HC	16.40	B	442	0.77	2.78	3.55	234	0.24	3.40	0.98	0.65	2.27	6.58	0.74	1.16	0.07	0.06	0.01	−25.32
SSK60787	MHD4	16.55	B	435	1.76	3.44	5.20	372	0.29	4.80	1.00	0.77	7.34	11.73	0.61	1.55	0.51	< LLD	–	−34.57
SSK60798	MHD4	20.18	B	430	0.94	3.60	4.54	222	0.41	2.00	0.89	0.75	1.78	1.09	0.38	3.72	0.65	0.55	0.04	−36.71
HC02_21	HC	22.02	B	439	0.70	2.52	3.22	210	0.34	2.37	0.99	0.77	2.77	12.01	0.81	2.12	< LLD	0.16	0.02	−36.50
HC02_23	HC	22.58	B	437	0.88	2.63	3.51	251	0.25	2.01	0.98	0.54	2.75	8.01	0.74	0.88	0.10	0.08	0.01	−28.79
HC02_25	HC	23.32	B	436	0.98	3.42	4.40	209	0.04	0.13	0.67	0.45	2.49	7.99	0.76	0.42	0.33	0.41	0.03	−33.06
SSK61404	C–S9	40.72	B	429	0.47	3.42	3.89	118	0.10	0.09	0.72	0.67	2.76	0.98	0.26	1.47	0.10	0.04	0.00	−32.13
SSK61412	C–S9	45.72	B	437	0.63	3.16	3.79	160	0.27	1.17	0.90	0.67	2.03	3.61	0.64	2.25	0.17	< LLD	–	−23.27
HC02_127	HC	62.78	B	433	0.93	3.99	4.92	196	0.06	0.15	1.00	0.73	1.64	2.49	0.60	2.56	< LLD	0.34	0.02	−37.23
HC02_172	HC	75.00	B	433	0.84	3.00	3.84	229	0.61	3.81	0.93	0.39	7.20	10.15	0.58	2.36	0.30	0.32	0.03	−35.11
HC02_173	HC	75.60	B	434	0.98	3.71	4.69	217	0.50	0.88	0.74	0.57	5.31	5.89	0.53	2.10	0.53	1.02	0.08	−34.59
HC02_174	HC	76.10	B	432	0.82	3.64	4.46	194	0.92	0.55	0.88	0.37	4.17	2.67	0.39	2.04	1.37	< LLD	0.00	−34.03
HC02_178	HC	77.67	B	434	0.80	3.05	3.85	209	0.40	0.37	0.57	0.57	2.53	1.63	0.39	1.46	0.44	1.53	0.14	−36.37
HC02_31	HC	25.52	C	441	1.03	3.30	4.33	242	0.15	0.66	0.94	0.65	2.41	7.38	0.75	0.97	0.09	0.19	0.02	−31.02
HC02_11	HC	5.90	D	436	0.33	1.85	2.18	143	0.48	3.56	0.91	0.73	1.78	1.10	0.38	2.61	0.21	0.19	0.03	−29.59
HC02_125	HC	62.44	D	437	0.29	1.30	1.59	181	0.33	3.19	1.00	0.55	3.82	2.18	0.36	1.19	0.13	0.11	0.02	−27.94
HC02_67	HC	44.77	E	431	0.37	1.90	2.27	152	0.50	1.07	0.81	0.73	2.64	1.34	0.34	2.88	0.12	0.93	0.15	−34.05
HC02_75	HC	48.82	E	442	0.26	1.45	1.71	153	0.31	0.81	0.73	0.63	1.34	0.97	0.42	1.23	0.09	0.44	0.09	−23.01
HC02_87	HC	51.86	E	435	0.66	3.11	3.77	185	0.32	0.89	0.80	0.73	2.25	1.26	0.36	2.71	0.52	0.50	0.05	−34.31
HC02_101	HC	54.70	E	439	0.47	1.96	2.43	191	0.21	0.17	0.92	0.70	1.26	1.52	0.55	1.48	0.05	0.08	0.01	−24.78
HC02_106	HC	56.35	E	439	0.56	2.89	3.45	173	0.45	1.26	0.75	0.60	1.72	1.01	0.37	2.07	0.12	0.63	0.06	−29.72
HC02_73	HC	48.14	Em	440	0.36	1.83	2.19	163	0.35	0.79	0.82	0.65	1.71	1.02	0.37	1.75	0.16	0.49	0.08	−28.52
HC02_120	HC	61.60	Em	437	0.24	1.37	1.61	162	0.02	0.06	0.75	0.75	0.28	1.20	0.81	0.51	< LLD	< LLD	–	−26.98
HC02_37	HC	28.70	F	440	0.78	2.97	3.75	196	0.04	0.13	0.95	0.74	1.79	5.87	0.77	0.97	0.20	< LLD	–	−34.64
HC01_10B	HC	33.58	F	432	0.65	3.46	4.11	152	0.00	0.08	0.83	0.68	3.08	1.46	0.32	3.58	0.74	1.18	0.10	−40.68
HC01_04B	HC	37.37	F	432	0.57	3.30	3.87	141	0.01	0.06	0.77	0.65	3.35	1.22	0.27	2.94	0.89	1.05	0.10	−40.10
HC02_62	HC	41.50	F	445	0.53	2.89	3.42	144	0.23	1.40	0.75	0.69	2.02	3.67	0.64	5.41	0.17	1.06	0.10	−40.81
SSK61420	C–S9	49.74	F	443	0.10	1.85	1.95	39	0.06	0.06	0.66	0.80	0.78	0.59	0.43	2.95	0.28	< LLD	–	−24.37
HC02_166	HC	72.02	F	433	0.47	3.04	3.51	130	0.04	0.11	0.91	0.79	1.30	0.73	0.36	3.27	0.08	0.27	0.03	−30.83
HC02_181	HC	79.31	F	432	0.33	2.82	3.15	104	0.14	0.12	0.95	0.76	1.87	1.48	0.44	3.35	0.28	0.46	0.05	−38.39
HC02_184	HC	80.83	F	432	0.53	3.56	4.09	135	0.07	0.11	0.90	0.73	4.46	1.53	0.26	3.66	0.24	0.91	0.08	−39.51
HC02_188	HC	83.60	G	440	0.68	2.63	3.31	232	0.07	0.09	0.51	0.78	1.21	1.12	0.48	1.93	0.12	1.56	0.17	−8.93
HC02_191	HC	85.70	G	440	0.41	2.27	2.68	169	0.06	0.09	0.31	0.74	1.04	1.04	0.50	1.23	0.26	2.56	0.34	6.41
SSK61352	C–S9	11.90	I	457	0.14	2.03	2.17	59	0.25	0.04	0.25	0.04	0.66	0.52	0.44	0.04	0.01	< LLD	–	−8.57

Notes: HC = Hind Clough, MHD4 = Marl Hill 4, Cominco S9 = C–S9.

*Fe_{mag} was excluded from Fe_{HR} for Facies H and I at Cominco S9, since Fe_{mag} is likely detrital in origin in these facies. Excluding Fe_{mag} from Fe_{HR} in these facies aligns the proxy with the other palaeoredox proxies (e.g., sedimentology, trace elements, S isotopes).

EF = Enrichment factor using PAAS (Taylor and McLennan, 1985). Sedimentary facies from Emmings et al. (2019a).

RockEval pyrolysis parameters: PC = pyrolised organic C, RC = residual organic C, TOC = total organic C, HI = hydrogen index, pyroMINC = pyrolised inorganic C, oxiMINC = oxidised inorganic C.

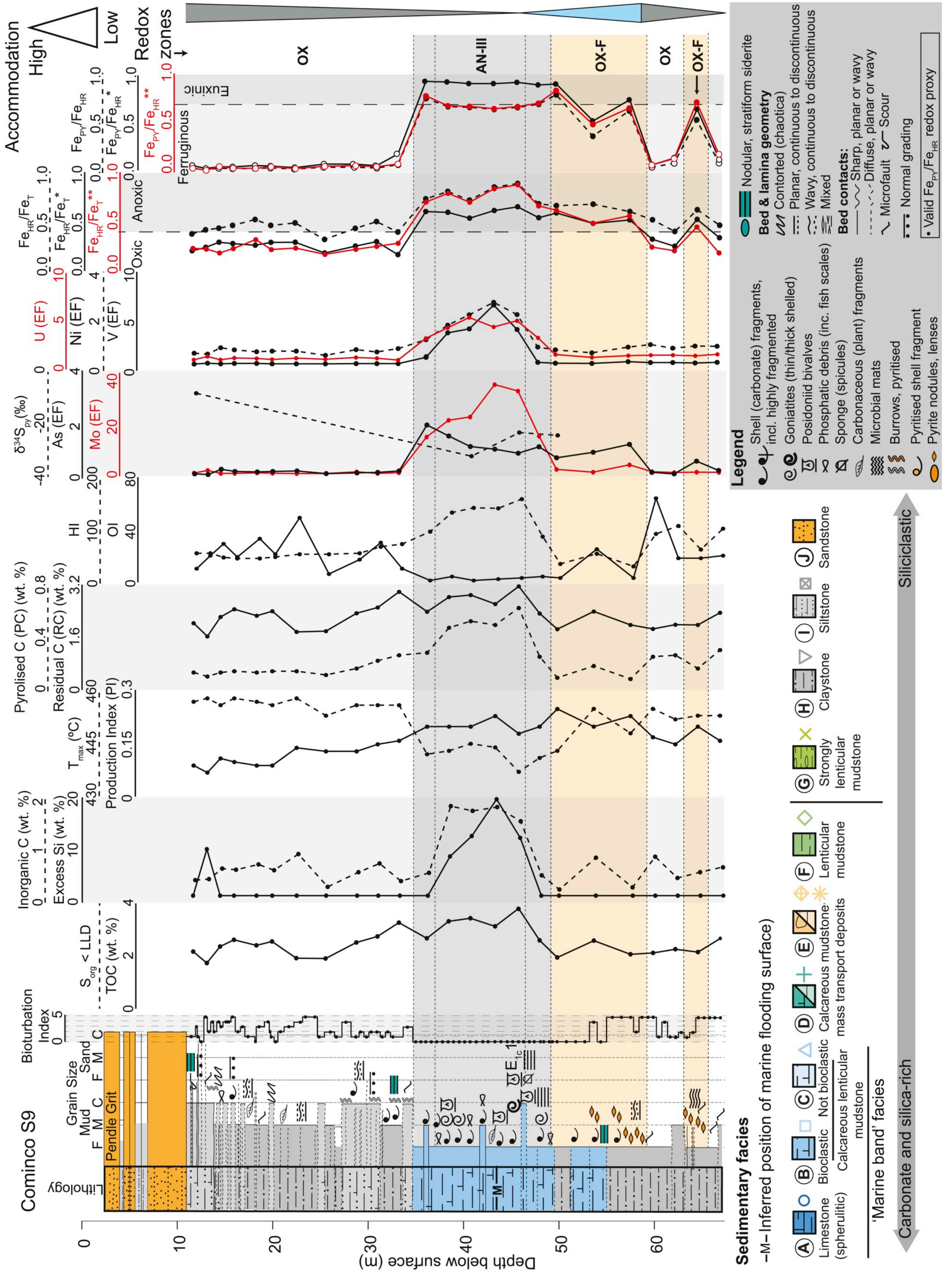

(Caption on next page)

Fig. 2. Sedimentary log, facies and bioturbation index through the Upper Bowland Shale, borehole Cominco S9, from Emmings et al. (2019a). Plotted with total organic carbon (TOC), inorganic C, excess Si and basin accomodation from Emmings et al. (2019a); organic S (S_{org}), RockEval pyrolysis T_{max}, Mo and U enrichment factors (EFs), $\delta^{34}S_{py}$, and Fe speciation (Fe_{HR}/Fe_T and Fe_{py}/Fe_{HR}) from Emmings et al. (2019b); RockEval pyrolysis production index (PI), pyrolised C (PC), residual C (RC), hydrogen index (HI), oxygen index (OI) and As, Ni and V (EFs) (this study). $^*Fe_{HR}$ excluding Fe_{carb}. $^{**}Fe_{HR}$ excluding Fe_{mag}, considered appropriate for Facies H–I samples because these likely contain a significant detrital Fe_{mag} fraction (i.e., Facies H–I are compositionally immature; see Emmings, 2018; Emmings et al., 2019a). Fe speciation palaeoredox fields from Poulton and Raiswell (2002) and Raiswell and Canfield (1998). See Results for definition of redox zones. Sedimentary facies key includes symbology on Figs. 4–7 and 9-11.

(Table 2; Fig. 4e). *n*-alkanes exhibit average Pr/C17, Pr/C18, Pr/Ph, Pr/(Pr + Ph), CPI_{25-34} and OEP_{21-25}, of 1.15, 0.75, 1.58, 0.61, 0.91 and 1.03, respectively (Table 2). Facies E samples tend to exhibit a slightly larger abundance of relatively long alkanes (C_{28} to C_{33}) and therefore higher ACL and TAR (Table 2), compared to the other facies (Fig. 4e).

4.2. *Palaeoredox zones*

Redox-sensitive trace elements, such as Mo, U, V and Ni, are enriched in all Facies A-F mudstones relative to PAAS (Figs. 2–3; Tables 1, 3 and 4; Emmings et al., 2019b). Facies G-I mudstones typically lack (or exhibit marginal) enrichment in redox-sensitive trace elements relative to PAAS. Fe_{HR}/Fe_T, Fe_{py}/Fe_{HR} and redox-sensitive trace element content are used to define seven 'redox zones' within these sedimentary packages (oxic-ferruginous, 'OX'; ferruginous-euxinic, 'AN', or; euxinic, 'EUX', bottom-waters). Suffixes I and III are an adaptation of V and Ni fixation pH-Eh regimes I and III of Lewan (1984). Zone EUX is equivalent to pH-Eh regime II of Lewan (1984) (see Discussion for further details). Zones EUX, AN-III, AN-I and AN-IT exhibit $Fe_{HR}/Fe_T > 0.38$, the threshold for delineation of anoxic conditions (Poulton and Canfield, 2011; Poulton and Raiswell, 2002; Raiswell and Canfield, 1998). These zones also exhibit Fe_{py}/Fe_{HR} typically 0.7–0.8, spanning the threshold for recognition of euxinic conditions (Poulton and Canfield, 2011; Poulton and Raiswell, 2002; Raiswell and Canfield, 1998). Therefore Emmings et al. (2019b) interpreted that these packages were deposited under anoxic, ferruginous and at least intermittently euxinic, conditions.

Zones OX-RX and OX-F exhibit Fe_{HR}/Fe_T close to 0.38 and minimal redox-sensitive trace element enrichment. Therefore these packages were deposited under (sub)oxic (RX) to ferruginous anoxic (F), but dominantly non-sulphidic, bottom-water conditions. Zone OX exhibits $Fe_{HR}/Fe_T < 0.38$ and lacks redox-sensitive trace element enrichment. Emmings et al. (2019b) suggested these packages were deposited under oxic to sub(oxic) conditions.

Redox-sensitive trace element fixation is largely coupled to the availability of free sulphide in bottom-waters and/or porewaters (e.g., Tribovillard et al., 2006). Therefore element EFs relative to the 'sulphidic' and 'non-sulphidic' (oxic to ferruginous) mean trace element concentrations (Table 3), rather than PAAS values, were utilised in order to delineate patterns of trace element enrichment. Thus EFs for samples deposited under at least intermittently sulphidic pore and/or bottom-waters (EUX, AN-III, AN-I and AN-IT zones) are based on the 'sulphidic' mean (Table 3; Fig. 5a, c, e). EFs for samples deposited under dominantly non-sulphidic, oxic to ferruginous conditions (OX-RX, OX-F and OX zones) are based on the 'non-sulphidic' mean (Fig. 5b, d, f).

Zone EUX defines Facies A-C samples with enrichment, to some degree, in all redox-sensitive trace elements (Figs. 5–6a, b), Fe_{HR}/FeT typically close to 1 and Fe_{py}/Fe_{HR} typically > 0.7 (Fig. 7b), and fine pyrite framboids and euhedra in the matrix (Fig. 8a; Emmings et al., 2019a, b). V, Se, Cr, Cu, Zn, Ba and Ni exhibit significant enrichment above the 'sulphidic' mean concentration (Table 3; Fig. 5a). Zone EUX is identified at the base of the $E_{1a}1$ marine band at MHD4 (Fig. 3b) and at the base of the $E_{1b}2$ marine band at Hind Clough (Fig. 3a). Zone AN-III defines Facies A-C and rarely F samples with significant V, Se and Cr enrichment and Ni, Pb, Co, Fe_T and As depletion relative to the 'sulphidic' mean (Table 3; Fig. 5c), elevated Mo enrichment compared to U (Fig. 6c), $Fe_{HR}/FeT > 0.38$ and highly variable Fe_{py}/Fe_{HR} (Fig. 7c), and fine framboidal pyrite in the sedimentary matrix (Fig. 8b). This zone overlies zone EUX in the $E_{1a}1$ marine band at MHD4 (Fig. 3b) and defines most Facies B–C (marine band) samples at Hind Clough (Fig. 3a) and Cominco S9 (Fig. 2).

Zone AN-I defines Facies F samples with Cu, Mo, Ni, Pb, Co, Fe_T and As enrichment and V, Se, Cr, Mg, Zn, Mn, Sc, C, P and Ca depletion relative to the 'sulphidic' mean (Table 3; Fig. 5e). Zone AN-I exhibits elevated Mo enrichment compared to U (Fig. 6d), $Fe_{HR}/FeT > 0.38$ and Fe_{py}/Fe_{HR} close to 0.75 (Fig. 7d). Zone AN-I samples also exhibit mixed microcrystalline and framboidal pyrite in the sedimentary matrix (Fig. 8c). This zone is present above the $E_{1a}1$ marine band, and above and below the $E_{1b}2$ marine band, at Hind Clough (Fig. 3a). Zone AN-IT exhibits trace element and Fe speciation enrichment patterns that is transitional between zones AN-III and AN-I (Figs. 5, 6e and 7e) but exhibits interlocking pyrite crysts along coarse mud to sand-sized laminae within Facies D-Em interbedded mass transport deposits at Hind Clough (Figs. 3a and 8d).

Zone OX-RX defines Facies G samples above the $E_{1b}2$ marine band at Hind Clough (Fig. 3a), with marginal enrichment in S, As, Sb, Se, U, Cu, V, Pb, Ni and Mo relative to the 'non-sulphidic' mean (Table 3; Fig. 5b). Zone OX-RX exhibits Mo and U enrichment that is proportional (in log-log space; Fig. 6f), Fe_{py}/Fe_{HR} close to 0.75 and Fe_{HR}/Fe_T close to 0.38 (Fig. 7f). Zone OX-RX contains pyritised burrows and relatively large framboids, aggregates and nodules (Fig. 3a; 8e; Emmings et al., 2019a). Zone OX-F defines several Facies H samples below the $E_{1c}1$ marine band at Cominco S9 (Fig. 2). This zone exhibits marginal enrichment in S, As and Pb relative to the 'non-sulphidic' mean, and slightly elevated enrichment in Mo compared to U (Fig. 6g). Zone OX-F also exhibits $Fe_{HR}/Fe_T > 0.38$ and Fe_{py}/Fe_T close to 0.7 (Table 3; Fig. 5d) and contains aggregated pyrite euhedra. Zone OX defines all other Facies H–I samples at Cominco S9 (Fig. 2), which exhibit redox-sensitive trace element depletion relative to the 'non-sulphidic' mean (Table 3; Fig. 5f), and proportionally low Mo and U content (Fig. 6h). Zone OX exhibits $Fe_{HR}/Fe_T < 0.38$ and $Fe_{py}/Fe_T < 0.25$, bioturbation and contains rare, scattered pyrite euhedra (Fig. 2; 8f).

4.3. *Integrated geochemistry*

Fe_{HR}/FeT and Fe_{py}/Fe_{HR} and V and Ni EFs readily delineate organic geochemical heterogeneity (Fig. 9a–b; 10a-b). Samples plot along a mixing line from Zone EUX (high Fe_{HR}/FeT, Fe_{py}/Fe_{HR} and high HI) to Zone OX (low Fe_{HR}/FeT, Fe_{py}/Fe_{HR} and low HI; Fig. 9a–b). Zones AN-I and OX-F deviate from this mixing line towards relatively low HI and moderate to high Fe_{HR}/FeT and Fe_{py}/Fe_{HR}. Inorganic C, and the ratio of pyrolised inorganic C (pyroMINC) to oxidised inorganic C (oxiMINC), versus HI also delineates most sedimentary facies and redox zones (Fig. 9c–d). Inorganic C and oxiMINC are highest in Facies A-B, moderate to low in Facies C-E and very low to trace in Facies F–I (Table 1, Figs. 2–3).

Zone EUX (Facies A-C) exhibits moderate to high enrichment in both V and Ni, and moderate to high HI (Fig. 10a–b). Zone AN-III (Facies A-C and rarely F) exhibits high V and low Ni enrichment, and relatively low to moderate HI. Zones AN-I and AN-IT (Facies D-F) exhibit low V and high Ni enrichment, and low HI. Zones OX and OX-F (Facies H–I) are depleted in both V and Ni, and exhibit low HI.

Zone AN-I (Facies F) mudstones have low $\delta^{34}S_{py}$ and low V/(V + Ni), and plot on two mixing lines, connecting zones EUX and

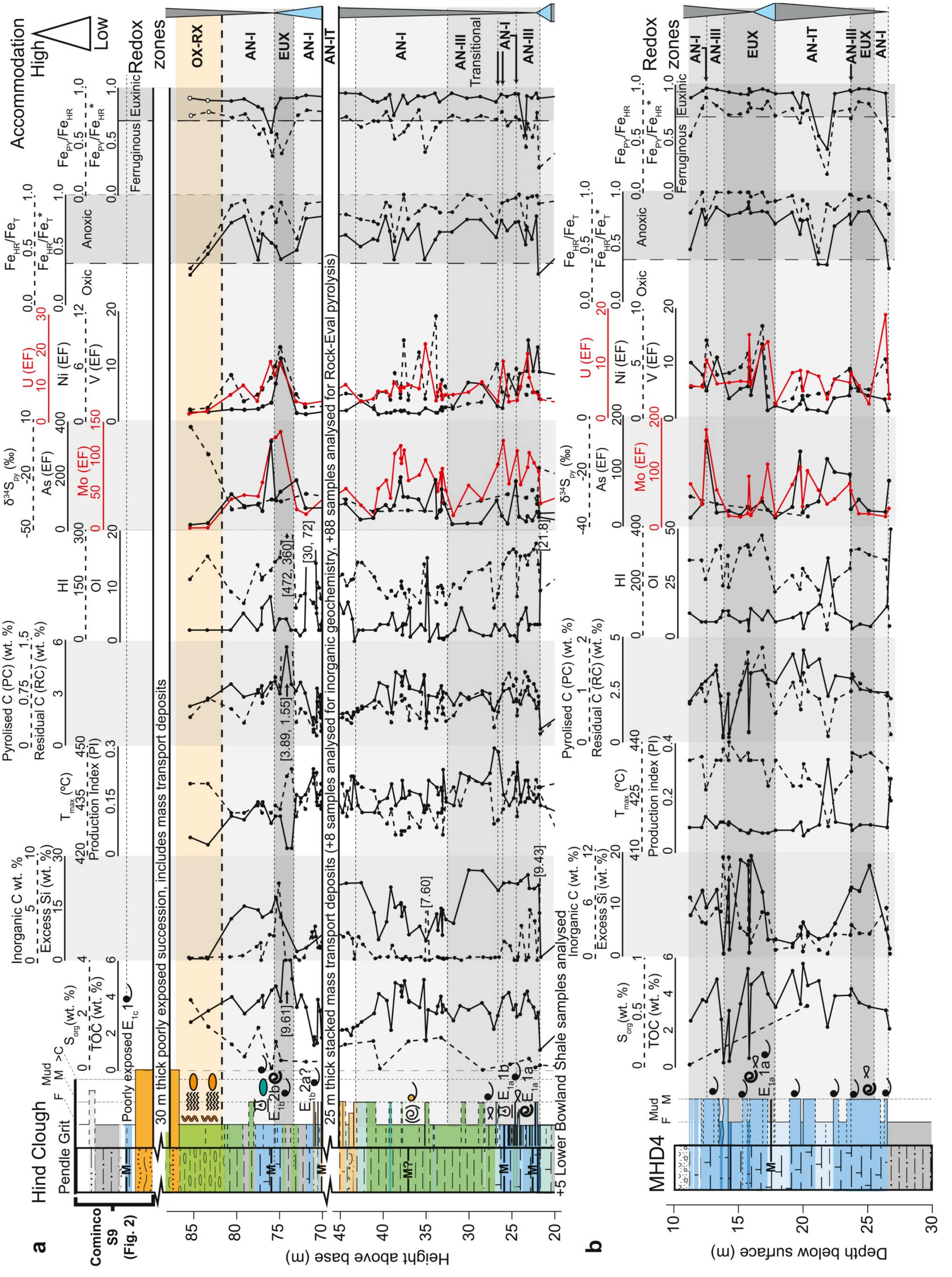

(Caption on next page)

Fig. 3. Sedimentary log, sedimentary facies and bioturbation index through the Upper Bowland Shale at outcrop Hind Clough (a) and in borehole MHD4 (b), from Emmings et al. (2019a). Plotted with total organic carbon (TOC), inorganic C, excess Si and basin accomodation from Emmings et al. (2019a); organic S (S_{org}), RockEval pyrolysis Tmax, Mo and U enrichment factors (EFs), $\delta^{34}S_{py}$, and Fe speciation (Fe/Fe_T and Fe_{py}/Fe_{HR}) from Emmings et al. (2019b); RockEval pyrolysis production index (PI), pyrolised C (PC), residual C (RC), hydrogen index (HI), oxygen index (OI) and As, Ni and V (EFs) (this study). $^*Fe_{HR}$ excludes Fe_{carb}. $^{**}Fe_{HR}$ excludes Fe_{mag}, considered appropriate for Facies H–I samples because these likely contain a significant detrital Fe_{mag} fraction (i.e., Facies H–I are compositionally immature; see Emmings, 2018; Emmings et al., 2019a). Fe speciation palaeoredox fields from Poulton and Raiswell (2002) and Raiswell and Canfield (1998). See Results for definition of redox zones. See Fig. 2 for key. TOC, inorganic C, PC, HI and OI values higher than the scale limits are labelled in [] parentheses.

AN-III (Facies A-C) with moderate $\delta^{34}S_{py}$ and high V/(V + Ni), and zones OX and OX-RX (Facies G-H) with high $\delta^{34}S_{py}$ and moderate high V/(V + Ni) (Fig. 10c). Zone AN-IT (Facies D-E) tends to exhibit variable V/(V + Ni) and low to moderate $\delta^{34}S_{py}$. Low V/Ni delineates S_{org}-rich Facies E-G (Fig. 10d).

Three Facies A limestone samples (from Zone EUX in MHD4) exhibit $\delta^{13}C_{carb}$ of −1.13, −7.83 and −1.49‰ and $\delta^{18}O_{carb}$ of −6.73, −5.70 and −6.38‰, respectively. Facies B mudstones have a mean $\delta^{13}C_{org}$ of −27.92‰ (± 2.47 2σ). This is similar to the Facies B-G average $\delta^{13}C_{org}$ of −28.16‰ (± 0.44 2σ). Facies H–I mudstones have a mean $\delta^{13}C_{org}$ of −25.86‰ (± 0.46 2σ). Facies A $\delta^{18}O_{carb}$ equates to an estimated calcite precipitation temperature between 20 and 37 °C, using the palaeotemperature equation of Kim and O'Neil (1997) and assumed $\delta^{18}O_w$ between −1.8‰ (Stephenson et al., 2010) and −4‰ (VSMOW) (see Discussion and Appendix F for further details).

5. Discussion

5.1. Organic matter type

Relatively high HI, high PC/RC and low OI suggests Facies A-G bulk organic matter (OM) is mixed Type II/III (e.g., Fig. 4b–d) (Espitalie et al., 1977; Tissot and Pelet, 1981). Several Facies B and D-G mudstones exhibit a bulk S_{org}/TOC molecular ratio of > 0.04, indicative of Type II-S kerogen (Fig. 10d) (Emmings et al., 2019b; Orr, 1986). Facies A-F *n*-alkane parameters TAR and ACL (Table 2) suggest the solvent-extractable OM is likely marine and algal in origin (Bourbonniere and Meyers, 1996; Peters et al., 2005). Slightly higher TAR and ACL in Facies E (Table 2; Fig. 4e) indicates an increased proportion of terrestrial OM. This is plausible considering Facies E are interpreted as a suite of subaqueous density flow deposits (Emmings et al., 2019a) expected to contain a greater component of allochthonous OM. On the basis of relatively low HI and high OI, Facies H–I bulk OM is interpreted as Type III OM (terrestrial OM such as wood supplied primarily from the Pendle

Table 2
Selected n-alkane parameters.

Sample	Location	Depth/Height [m]	Facies	Pr/n-C17	Ph/n-C18	Pr/Ph	Pr/(Pr + Ph)	TAR	ACL	CPI_{25-34}	OEP_{21-25}
HC02_20	HC	21.8	A	1.59	0.97	1.83	0.65	0.00	18.29	1.14	1.04
HC02_2	HC	0.68	B	1.19	0.69	1.80	0.64	0.12	18.86	0.91	1.04
SSK60774	MHD4	12.9	B	1.77	0.89	2.06	0.67	0.13	18.73	0.89	1.02
HC02_14	HC	12.9	B	1.34	0.82	1.79	0.64	0.04	17.74	0.79	1.05
SSK60787	MHD4	16.55	B	1.20	0.61	2.06	0.67	0.07	17.77	0.82	1.01
SSK60788	MHD4	16.99	B	0.95	0.64	1.52	0.60	0.10	19.41	1.09	1.00
HC02_23	HC	22.58	B	1.35	0.75	1.65	0.62	0.16	19.49	0.93	1.05
HC02_25	HC	23.32	B	1.87	1.07	1.61	0.62	0.15	19.51	0.83	1.01
HC02_27	HC	24.16	B	1.41	0.80	1.68	0.63	0.13	19.22	0.90	1.03
SSK60772	MHD4	12.06	C	1.88	0.92	1.99	0.67	0.15	18.85	0.83	1.02
SSK60781	MHD4	14.8	C	1.48	0.75	2.12	0.68	0.11	18.69	0.90	1.02
HC02_31	HC	25.52	C	1.03	0.62	1.69	0.63	0.15	19.00	0.91	1.03
HC02_32	HC	26.2	C	0.80	0.53	1.60	0.62	0.06	17.93	0.87	1.02
HC02_11	HC	5.9	D	0.71	0.52	1.50	0.60	0.05	18.34	0.91	1.03
HC02_49A	HC	35.37	D	0.96	0.78	1.53	0.60	0.00	16.40	1.31	1.00
HC02_58	HC	39.5	D	1.02	0.82	1.38	0.58	0.11	18.64	0.83	1.03
HC02_63	HC	43	D	1.15	0.82	1.37	0.58	0.18	19.82	0.94	1.03
HC02_67	HC	44.77	E	0.95	0.68	1.38	0.58	0.19	19.65	0.89	1.01
HC02_75	HC	48.82	E	1.02	0.72	1.44	0.59	0.21	19.88	0.96	1.02
HC02_73	HC	48.14	Em	1.20	0.79	1.43	0.59	0.22	19.89	0.95	1.01
HC02_33	HC	26.83	F	0.97	0.66	1.22	0.55	0.13	19.70	0.87	1.02
HC02_37	HC	28.7	F	0.96	0.67	1.56	0.61	0.06	17.99	0.98	1.02
HC02_40	HC	30.3	F	1.18	0.73	1.61	0.62	0.08	18.53	0.90	1.03
HC02_43	HC	32.1	F	1.03	0.70	1.44	0.59	0.07	18.49	1.01	1.03
HC01_10B	HC	33.58	F	0.95	0.85	1.29	0.56	0.01	17.61	0.79	1.05
HC02_51	HC	36.1	F	1.01	0.78	1.28	0.56	0.03	18.44	0.75	1.03
HC01_04B	HC	37.37	F	0.84	0.75	1.42	0.59	0.01	17.00	0.71	1.12
HC02_57	HC	39	F	0.95	0.80	1.34	0.57	0.05	18.28	0.80	1.03
HC02_61	HC	40.95	F	0.79	0.61	1.38	0.58	0.04	18.44	0.92	1.01
HC02_62	HC	41.5	F	0.93	0.67	1.43	0.59	0.09	19.09	0.84	1.02
Average				**1.15 (± 0.62)**	**0.75 (± 0.25)**	**1.58 (± 0.49)**	**0.61 (± 0.07)**	**0.10 (± 0.12)**	**18.66 (± 1.71)**	**0.91 (± 0.24)**	**1.03 (± 0.04)**

Notes: Sedimentary facies from Emmings et al. (2019a).

Table 3
Summary of mean and 2σ major and trace element concentration data.

Major (wt. %)	n	Si	Ti	Al	Fe	Mn	Mg	Ca	Na	K	P	S	C
Mean (all)	109	25.11 ± 8.21	0.32 ± 0.11	7.55 ± 2.54	3.63 ± 2.9	0.04 ± 0.05	1.03 ± 1.49	5.29 ± 6.14	0.14 ± 0.11	1.42 ± 0.54	0.12 ± 0.23	2.50 ± 2.52	4.53 ± 2.13
Mean (sulphidic)	88	25.57 ± 10.39	0.22 ± 0.12	4.84 ± 2.72	3.20 ± 3.52	0.04 ± 0.06	1.18 ± 2	7.77 ± 8.33	0.14 ± 0.09	1.15 ± 0.59	0.13 ± 0.29	2.65 ± 2.87	5.49 ± 2.59
Mean (non-sulphidic)	21	24.18 ± 2.38	0.54 ± 0.09	12.98 ± 2.05	4.50 ± 1.24	0.02 ± 0.02	0.73 ± 0.14	0.32 ± 0.29	0.14 ± 0.15	1.95 ± 0.38	0.09 ± 0.05	2.18 ± 1.56	2.61 ± 0.9
Trace (ppm)	**n**	**As**	**Ba**	**Ce**	**Co**	**Cr**	**Cs**	**Cu**	**Ga**	**La**	**Mo**	**Nb**	**Nd**
Mean (all)	107	35.30 ± 47.3	241.10 ± 131.2	68.20 ± 29.4	19.10 ± 14.7	91.20 ± 62.9	16.30 ± 10	48.20 ± 30.4	18.10 ± 6.9	34.60 ± 14.7	18.20 ± 20.8	10.60 ± 3.5	33.70 ± 16.4
Mean (sulphidic)	86	41.70 ± 53.8	228.10 ± 162.4	48.20 ± 30.8	16.50 ± 17.2	72.30 ± 63.6	12.90 ± 10	50.20 ± 36	11.50 ± 7	25.90 ± 15.4	25.10 ± 26	7.90 ± 3.8	26.50 ± 17.2
Mean (non-sulphidic)	21	22.40 ± 30.1	267.10 ± 48.1	108.20 ± 25.7	24.20 ± 8.1	128.90 ± 61.1	23.00 ± 9.9	44.30 ± 15.5	31.30 ± 6.7	52.20 ± 13	4.40 ± 7.1	16.20 ± 2.6	48.10 ± 14.3
Trace (ppm)	**n**	**Ni**	**Pb**	**Rb**	**Sb**	**Sc**	**Se**	**Sr**	**Th**	**U**	**V**	**Y**	**Zn**
Mean (all)	107	72.90 ± 50.7	78.10 ± 92.8	84.90 ± 33	5.60 ± 5.9	16.80 ± 8.6	15.90 ± 24.4	236.10 ± 189.9	8.80 ± 3.1	9.30 ± 6.6	212.80 ± 200.2	29.30 ± 19.1	77.80 ± 175.4
Mean (sulphidic)	86	70.70 ± 60	94.90 ± 117.4	68.50 ± 37.8	7.40 ± 5.9	16.10 ± 10.7	22.30 ± 31.1	261.50 ± 224.4	5.80 ± 3.2	10.50 ± 7.5	233.20 ± 258.9	29.20 ± 23.5	93.00 ± 231.4
Mean (non-sulphidic)	21	77.30 ± 25.8	44.60 ± 27.2	117.70 ± 20.2	2.00 ± 6	18.20 ± 3.3	3.00 ± 6.6	185.20 ± 97.8	14.70 ± 2.6	6.80 ± 4.2	172.00 ± 43.8	29.40 ± 7.5	47.60 ± 26

Notes: 'Sulphidic': Facies A-F. 'non-sulphidic': Facies G-I. Sedimentary facies from Emmings et al. (2019a).

delta; Fig. 4b–c).

Reversal in T_{max} through the $E_{1c}1$ marine band (Fig. 2) is most likely due to a change in OM type, from terrestrial (gas-prone, high T_{max}) to marine (oil-prone, low T_{max}) (e.g., Tissot and Welte, 1984). Alternatively, changing clay mineralogy, from mica, chlorite and kaolinite-rich Facies H–I, to illite and/or illite-smectite-rich Facies B in the $E_{1c}1$ marine band (Emmings et al., 2019a), potentially promoted hydrocarbon retention (Espitalie et al., 1980) or catalysed thermal maturation (Bu et al., 2017) as 'matrix effects'.

Mississippian amorphous OM (AOM; of probable marine origin) exhibits an average $\delta^{13}C_{org}$ of −29.1‰ (Lewan, 1986), whereas terrestrial OM typically exhibits −23.9‰ (Peters-Kottig et al., 2006) to −25.1‰ $\delta^{13}C_{org}$ (Könitzer et al., 2016). Therefore $\delta^{13}C_{org}$ is a proxy for the bulk OM composition (e.g., Stephenson et al., 2008; Könitzer et al., 2016; Hennissen et al., 2017). The Facies B-G $\delta^{13}C_{org}$ average of −28.2‰ corroborates the interpretation that OM in these mudstones is dominantly marine and/or bacterial in origin, which is mixed with subordinate terrestrial OM. Similarly, Facies H–I mean $\delta^{13}C_{org}$ = −25.9‰ supports the interpretation that OM in these facies is dominantly terrestrial in origin.

5.2. Syngenetic and early diagenetic processes

Coupling of bottom-water anoxia and presence of aerobic and euhaline fauna which likely inhabited the euphotic zone, such as radiolaria (e.g., Casey, 1993), suggests the Craven Basin was primarily

Table 4
Summary of mean and 2σ major and trace element enrichment factors (using PAAS).

Major (wt. %)	n	Si	Ti	Al	Fe	Mn	Mg	Ca	Na	K	P	S	C
Mean (all)	109	1.5 ± 1	0.7 ± 0.1	1.0 ± 0	1.3 ± 1.4	1.8 ± 2.6	2.5 ± 3.3	70.7 ± 128	0.3 ± 0.3	0.7 ± 0.2	5.2 ± 13.7	75.3 ± 97.9	77.9 ± 116
Mean (sulphidic)	88	1.9 ± 1.3	0.7 ± 0.2	1.0 ± 0	1.5 ± 1.8	2.6 ± 3.5	3.5 ± 4.5	105.9 ± 175.9	0.4 ± 0.4	0.8 ± 0.2	7.4 ± 18.7	100.1 ± 124.7	113.9 ± 158.6
Mean (non-sulphidic)	21	0.6 ± 0.2	0.7 ± 0.1	1.0 ± 0	0.7 ± 0.3	0.2 ± 0.2	0.4 ± 0.1	0.3 ± 0.4	0.1 ± 0.2	0.5 ± 0.1	0.8 ± 0.4	25.7 ± 26.2	6.1 ± 2.4
Trace (ppm)	**n**	**As**	**Ba**	**Ce**	**Co**	**Cr**	**Cs**	**Cu**	**Ga**	**La**	**Mo**	**Nb**	**Nd**
Mean (all)	107	41.20 ± 56.7	0.70 ± 0.7	1.20 ± 0.6	1.20 ± 1.3	1.30 ± 1.1	1.50 ± 0.9	1.70 ± 1.2	1.10 ± 0.2	1.30 ± 0.7	39.20 ± 48.1	0.80 ± 0.2	1.60 ± 1.1
Mean (sulphidic)	86	56.10 ± 69.9	0.80 ± 0.9	1.30 ± 0.7	1.40 ± 1.6	1.50 ± 1.3	1.60 ± 1.1	2.20 ± 1.5	1.10 ± 0.3	1.50 ± 0.8	56.90 ± 63.3	0.80 ± 0.3	1.90 ± 1.4
Mean (non-sulphidic)	21	11.50 ± 21.5	0.30 ± 0.1	1.00 ± 0.2	0.80 ± 0.4	0.90 ± 0.6	1.10 ± 0.4	0.60 ± 0.3	1.10 ± 0.1	1.00 ± 0.2	3.60 ± 7.8	0.60 ± 0.1	1.10 ± 0.3
Trace (ppm)	**n**	**Ni**	**Pb**	**Rb**	**Sb**	**Sc**	**Se**	**Sr**	**Th**	**U**	**V**	**Y**	**Zn**
Mean (all)	107	2.30 ± 2.2	8.20 ± 14.3	0.80 ± 0.2	63.80 ± 59	4.40 ± 10.7	0.80 ± 1.1	3.30 ± 5.3	0.80 ± 0.3	5.70 ± 5.2	2.90 ± 2.3	2.00 ± 1.9	2.50 ± 7.3
Mean (sulphidic)	86	2.90 ± 2.8	11.40 ± 19	0.90 ± 0.3	91.50 ± 70.4	6.10 ± 14.7	1.20 ± 1.5	4.70 ± 7.2	0.80 ± 0.3	7.70 ± 6.7	3.90 ± 3.1	2.60 ± 2.5	3.60 ± 9.9
Mean (non-sulphidic)	21	1.00 ± 0.5	1.70 ± 1.6	0.60 ± 0.1	8.40 ± 28.7	0.80 ± 0.1	0.00 ± 0.1	0.70 ± 0.3	0.70 ± 0.1	1.60 ± 1.2	0.80 ± 0.2	0.80 ± 0.2	0.40 ± 0.2

Notes: 'Sulphidic': Facies A-F. 'non-sulphidic': Facies G-I. Sedimentary facies from Emmings et al. (2019a).

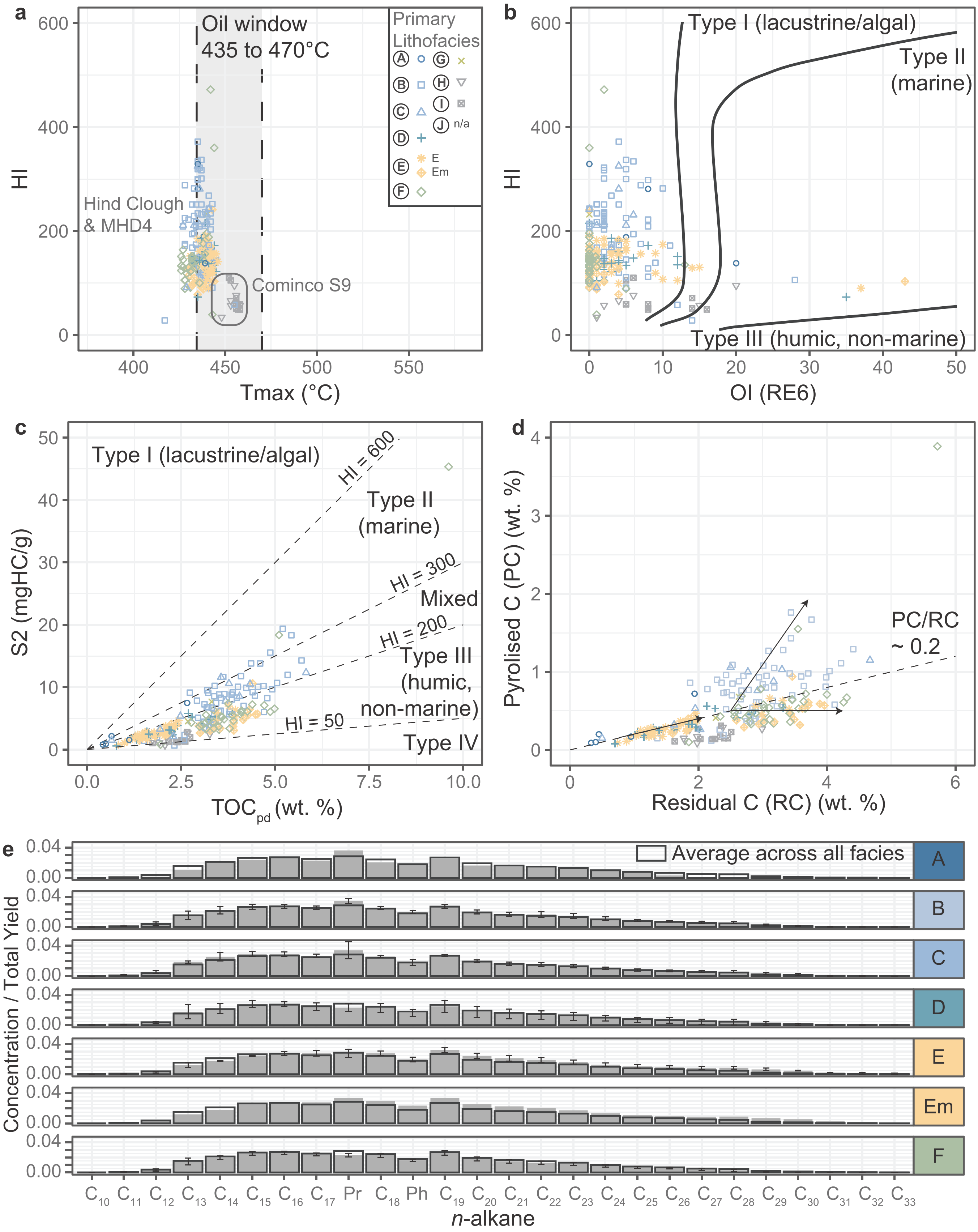

Fig. 4. RockEval pyrolysis (a–d) and n-alkane biomarker analyses (e). a) Hydrogen index (HI) versus T_{max} plotted with typical 'oil window' range. b) HI versus oxygen index (OI) pseudo-van Krevelen plot with typical maturation pathways. c) S2 versus total organic carbon (TOC, present day) with typical Type I-IV OM compositional fields (e.g., Tissot and Pelet, 1981). d) Pyrolised C (PC) versus residual C (RC), PC/RC delineates most Facies A-C and Facies D-I samples. e) n-alkane concentration data normalised to the total yield for Facies A-F, including average across all facies, and 2σ facies-specific population uncertainty where applicable. See (a) for key to sedimentary facies.

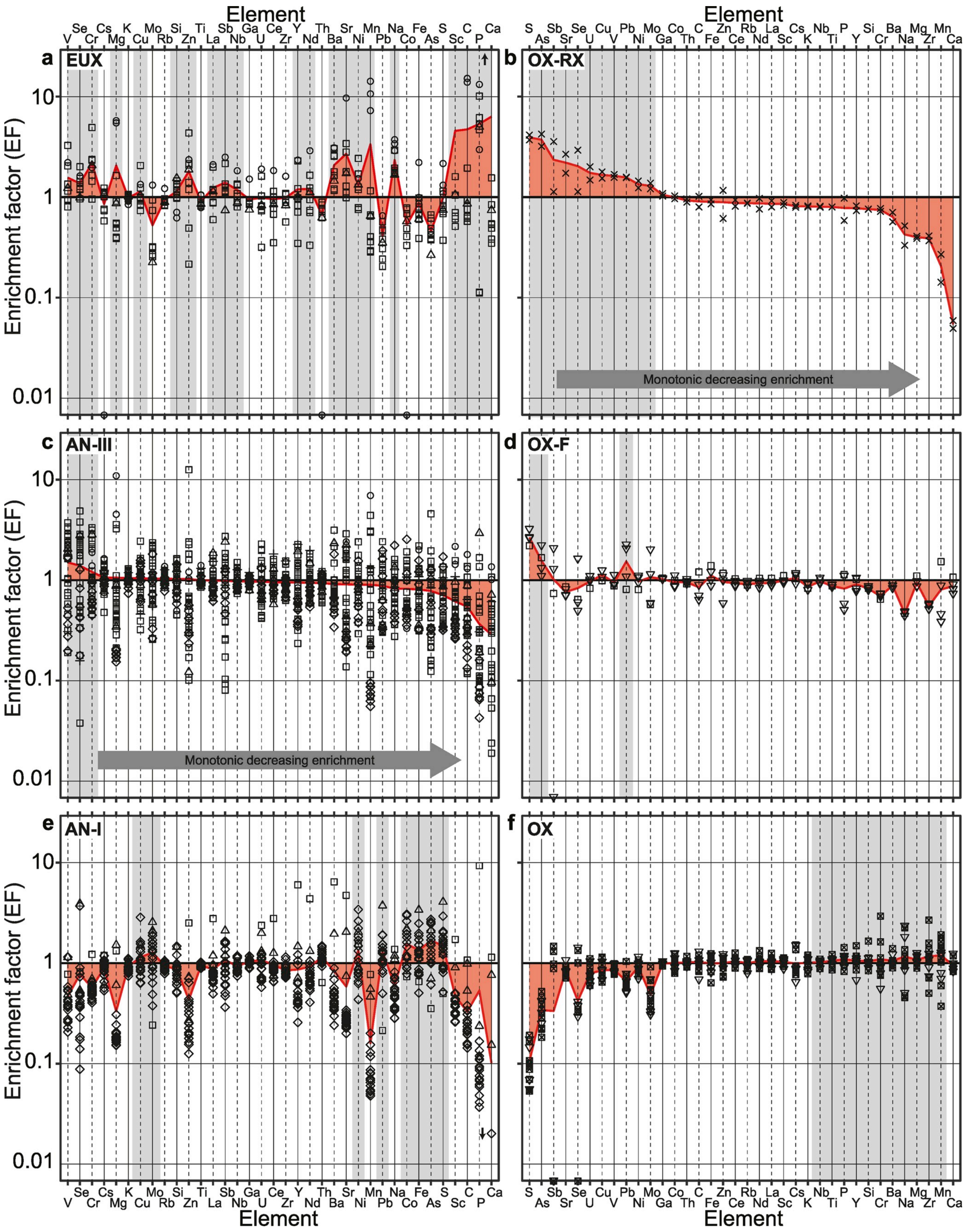

Fig. 5. Trace element enrichment factors (EFs) using mean 'sulphidic' element concentrations for redox zones EUX, AN-III and AN-I (a, c, e) and mean 'non-sulphidic' (oxic-ferruginous) element concentrations for redox zones OX-RX, OX-F and OX (b, d, f). Elements are ordered as a monotonic decrease in element enrichment in zones AN-III (a, c, e) and OX-RX (b, d, f), respectively. See Results for definition of redox zones and Table 3 for mean concentration data. See Fig. 4a for sedimentary facies key. Element distribution in Zone AN-IT (not shown) is transitional between zones AN-III and AN-I.

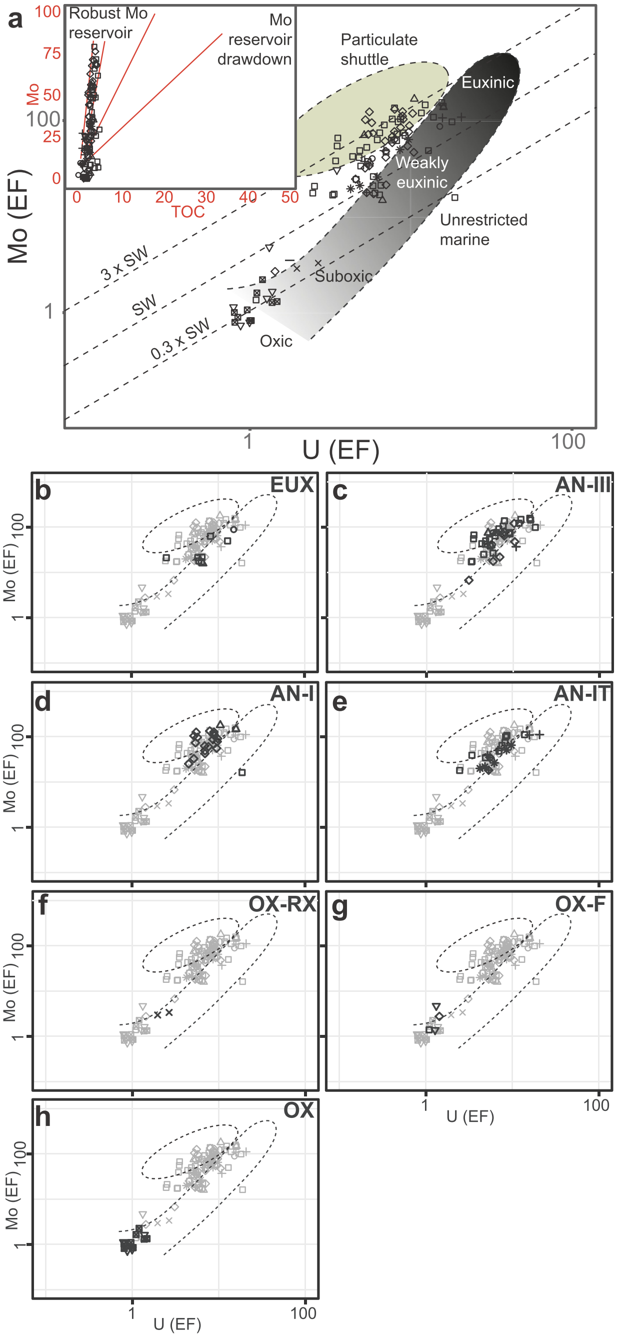

Fig. 6. Mo and U enrichment factors (EFs) plotted for sedimentary facies (a) and redox zones EUX, AN-III, AN-I, AN-IT, OX-RX, OX-F and OX (b–h), respectively. Mo versus U palaeoredox fields from Tribovillard et al. (2012). Mo/TOC (a, subset) fields from Algeo and Lyons (2006). See Fig. 4a for sedimentary facies key. The SW line represents the present-day Mo/U molar ratio of seawater (SW) of 3.1, as defined by Tribovillard et al. (2012). Multiples of the modern SW Mo/U line (0.3x, 3x) are also plotted.

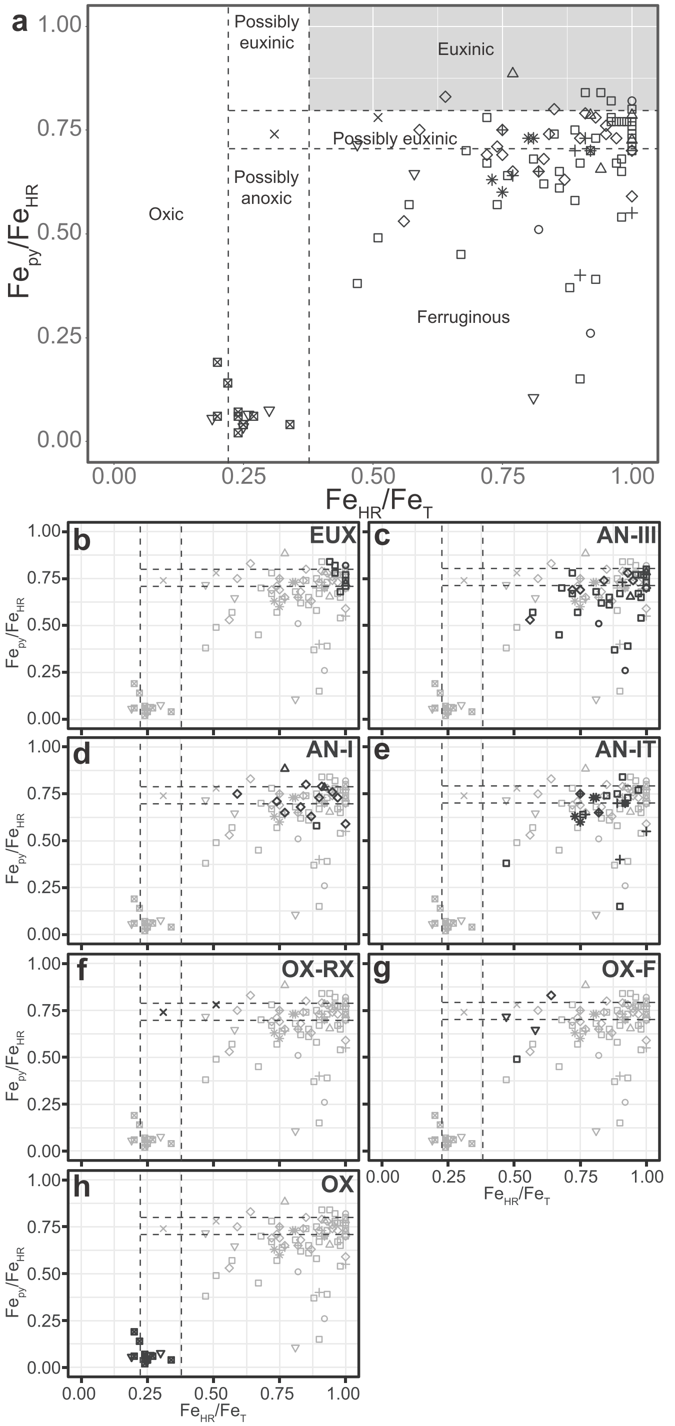

Fig. 7. Fe_{HR}/Fe_T and Fe_{py}/Fe_{HR} cross-plot for sedimentary facies (a) and redox zones EUX, AN-III, AN-I, AN-IT, OX-RX, OX-F and OX (b–h), respectively, with palaeoredox fields from Poulton and Canfield (2011) after Poulton and Raiswell (2002) and Raiswell and Canfield (1998). *Facies H–I Fe_{HR} excludes Fe_{mag} because these facies likely contain a significant detrital Fe_{mag} fraction (i.e., Facies H–I are compositionally immature; see Emmings, 2018; Emmings et al., 2019a). See Fig. 4a for sedimentary facies key.

temperature-stratified (i.e., a freshwater lid, if present, did not directly overlie anoxic waters). The Craven Basin was apparently only weakly restricted (i.e., connected to a much larger marine reservoir), on the basis of high Mo/TOC (Algeo and Lyons, 2006) and Mo and U EFs (Tribovillard et al., 2012) indicate a relatively short deep water residence time (Fig. 6a). The Cariaco Basin (offshore Venezuela) is a potential modern analogue. Bottom-water and porewater anoxia fixed a variety of redox-sensitive trace elements in the sediment (typically '2+' cations when reduced, such as Cu, Ni, Mo, Zn, As, Pb, Co, but also U, V, Cr; e.g., Figs. 2–3; 5; e.g., Tribovillard et al., 2006). Free sulphide induces low redox-potentials (Eh) that promote reduction of many redox-sensitive trace element species (see Tribovillard et al., 2006). Reduction reactions are also pH dependent and therefore some reactions are acid-catalysed, including via active surface minerals, such as kaolinite (Erickson and Helz, 2000). The degree of fixation of redox sensitive trace elements is therefore dependent on bottom and pore

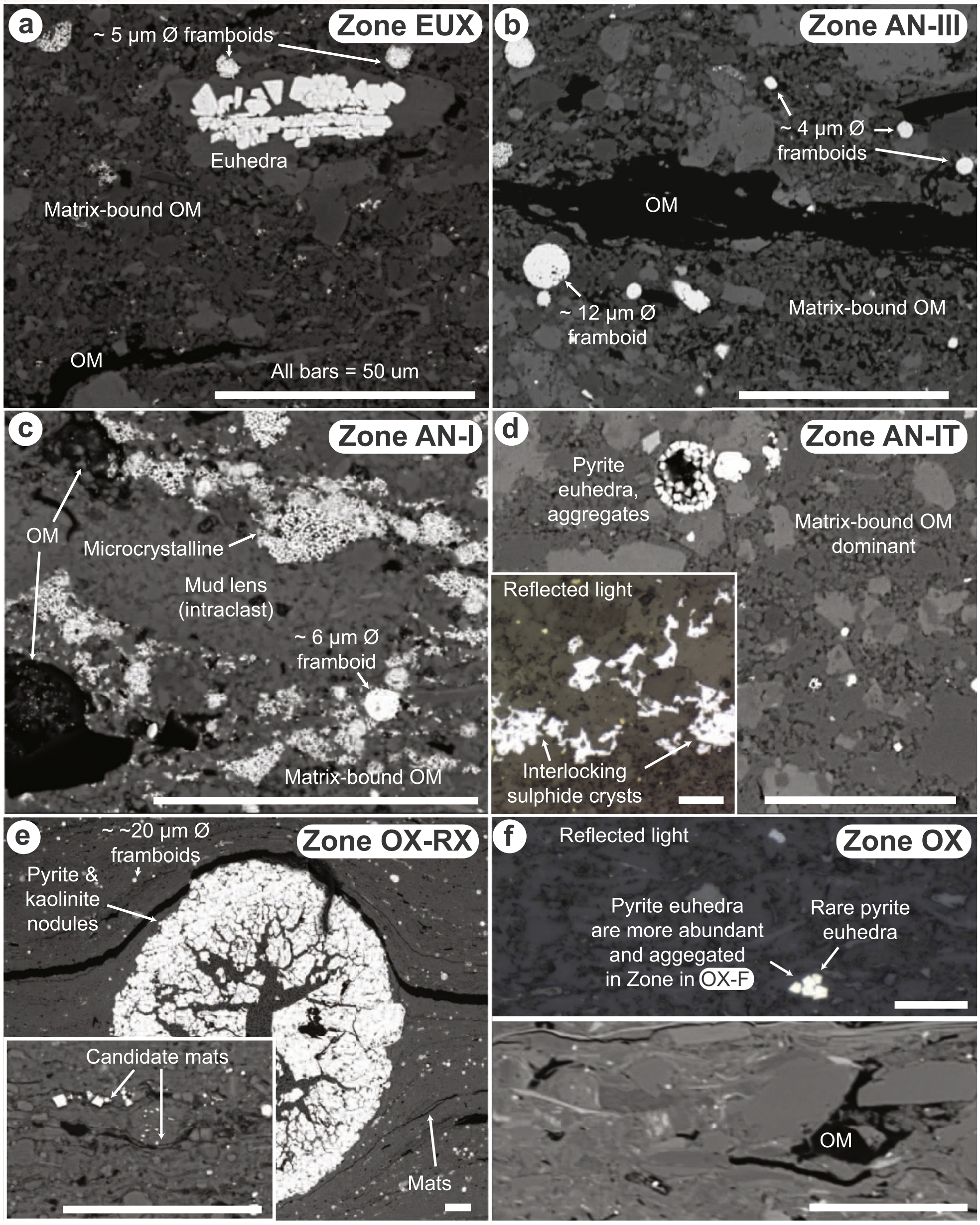

Fig. 8. Scanning electron (a–f) and reflected light (d and f, insets) microphotographs for redox zones EUX, AN-III, AN-I, AN-IT, OX-RX and OX (b–f), respectively.

water Eh and pH conditions, and is potentially a proxy for the stability of early diagenetic redoxclines.

5.3. Zone EUX: euxinic conditions

Enrichment in all redox-sensitive trace elements in Zone EUX (Fig. 5a) is interpreted to indicate persistently euxinic bottom-waters (i.e., 'stable' chemocline). This is supported by Fe_{py}/Fe_{HR} consistently close to 0.8 in Zone EUX (Figs. 7b and 9b; Emmings et al., 2019b), the upper threshold for identification of persistent water column euxinia (Poulton and Canfield, 2011; Poulton and Raiswell, 2002; Raiswell and Canfield, 1998). Low Eh and abundant supply of carriers for trace elements in bottom-waters (e.g., sulphide, OM) negated competition for fixation. This is analogous to Regime II of Lewan (1984). Relatively low Mo/U in Zone EUX (Figs. 2–3; 6b; Emmings et al., 2019b) also suggests the Fe–Mn oxyhydroxide 'particulate shuttle' to seabed was relatively weak (Tribovillard et al., 2012), consistent with the interpretation that the chemocline was positioned permanently in the water column.

The $\delta^{34}S_{py}$ record in Zone EUX is also consistent with euxinic conditions. Bacterial sulphate reduction to sulphide depletes seawater sulphate ^{32}S relative to ^{34}S (Chambers et al., 1975; Habicht and Canfield, 1997; Kaplan and Rittenberg, 1964; Kemp and Thode, 1968). $\delta^{34}S_{py}$ and $\delta^{34}S_{seawater}$ values in an anoxic Phanerozoic open system are typically offset by up to ~48‰, although larger fractionations are possible (e.g., up to 70‰; Canfield and Teske, 1996; Canfield et al., 2010). Therefore sedimentary $\delta^{34}S_{py}$ indicates whether pyrite formed in an open system, via exchange with seawater sulphate during syngenesis or early diagenesis, or within a 'closed system' (usually relatively late diagenesis; e.g., Nissenbaum et al., 1972; Mossmann et al., 1991; Canfield et al., 1992). Pendleian seawater sulphate $\delta^{34}S$ was ~13.0‰ (Kampschulte et al., 2001), indicating $\delta^{34}S_{py}$ of −40 to −30‰ in Zone EUX (Fig. 10c) represents a significant offset with the contemporaneous seawater sulphate. This suggests precipitation of pyrite in a (semi)-open system. Abundant fine framboids (with ~5 µm Ø) in Zone EUX also supports the interpretation of euxinic conditions (Fig. 8a) (Emmings et al., 2019a).

Zones EUX Facies A limestone $\delta^{18}O_{carb}$ and $\delta^{13}C_{carb}$ data plot on a mixing line between contemporaneous biogenic carbonate (Mii et al.,

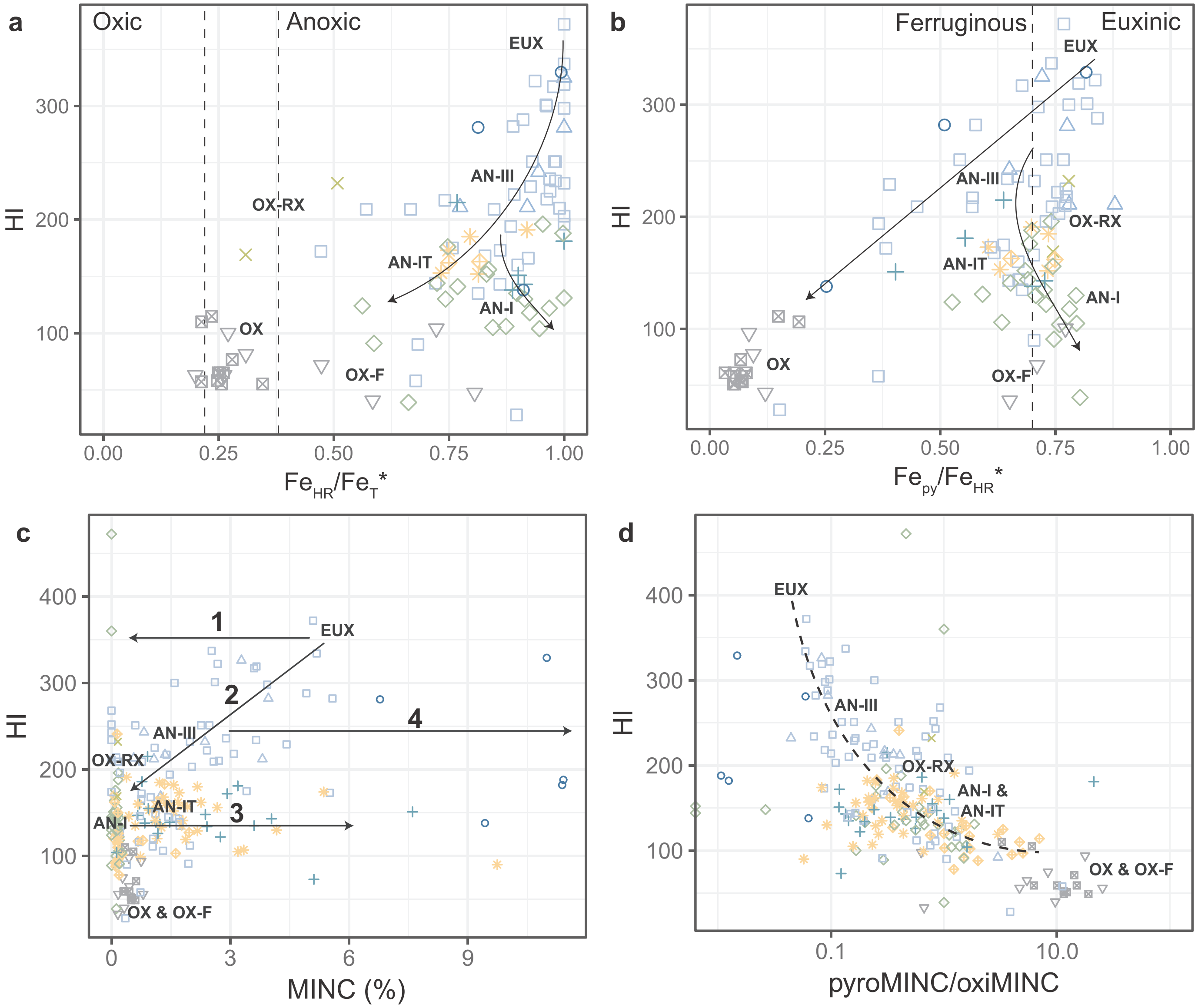

Fig. 9. Integrated organic and inorganic geochemistry. a) Hydrogen index (HI) versus Fe_{HR}/Fe_T plotted with sedimentary facies and approximate positions of each redox zone. b) HI versus Fe_{py}/Fe_{HR} plotted with sedimentary facies and approximate positions of each redox zone. *Facies H–I Fe_{HR} excludes Fe_{mag} because these facies likely contain a significant detrital Fe_{mag} fraction (i.e., Facies H–I are compositionally immature; see Emmings, 2018; Emmings et al., 2019a). c) HI versus inorganic C (MINC, measured via RockEval pyrolysis) content plotted with sedimentary facies and approximate positions of each redox zone. See Discussion for description of pathways 1–4. d) HI versus the ratio of pyrolised inorganic C (pyroMINC) to oxidised inorganic C (oxiMINC) measured via RockEval pyrolysis, plotted with sedimentary facies and approximate positions each redox zone. pyroMINC/oxiMINC is used as an approximation for the ratio of siderite to calcite and/or dolomite. See Fig. 4a for sedimentary facies key.

2001; Stephenson et al., 2010) and a relatively low $\delta^{18}O$ composition, comparable to modern authigenic carbonates associated with anaerobic methane oxidation (AMO; Appendix F) (Loyd et al., 2016; Mazzini et al., 2004) and/or dissolved inorganic C sourced from local degradation of $\delta^{13}C_{org}$ (e.g., Claypool and Kaplan, 1974). Assuming a mixture of locally dissolved unaltered or slightly altered primary carbonate and/or seawater ($\delta^{18}O_{carb} = -6.81‰$, $\delta^{13}C_{carb} = 0‰$), and carbonate sourced from AMO ($\delta^{18}O_{carb} = 0‰$, $\delta^{13}C_{carb} = -47‰$), this equates to 2%, 8% and 17% contributions to Facies A limestones using dissolved inorganic C derived from AMO (see Appendix F). These values are consistent with the fraction of AMO-derived dissolved inorganic C in several modern and ancient methane seeps (Joseph et al., 2013; Loyd et al., 2016; Nesbitt et al., 2013; Tong and Chen, 2012).

Early diagenetic porewaters likely inherited a composition between $\delta^{18}O_w = -1.8‰$ VSMOW (Stephenson et al., 2010) and $-4.3‰$ VSMOW (due to biogenic silica recrystallization; see Appendix F for details). Using the palaeotemperature equation of Kim and O'Neil (1997), a bottom-water temperature of 18 °C as observed in the modern Cariaco Basin (Alvera-Azcárate et al., 2011) and a local basinal geotherm of 24 °C/km during the Carboniferous (based on the nearby Thistleton-1 well; Andrews, 2013), this suggests Facies A limestones formed between ~775 m (assuming $\delta^{18}O_w = -1.8‰$ VSMOW) and ~31 m (assuming $\delta^{18}O_w = -4.3‰$ VSMOW) below seafloor. Spherules likely precipitated within ~800 ka, on the basis this is the estimated timespan of deposition from $E_{1a}1$ to the top of the (several hundreds of metres thick) overlying Pendle Grit (Waters and Condon, 2012; Waters et al., 2009).

Two key observations favour a relatively shallow depth of spherule precipitation closer to ~31 m (i.e., significantly shallower than 775 m). Firstly, the radial, fan-shaped spherule geometry (Emmings et al., 2019a) suggests precipitation under minimal overburden stress. Secondly, high biogenic silica content and quartz cement infilling shelter-

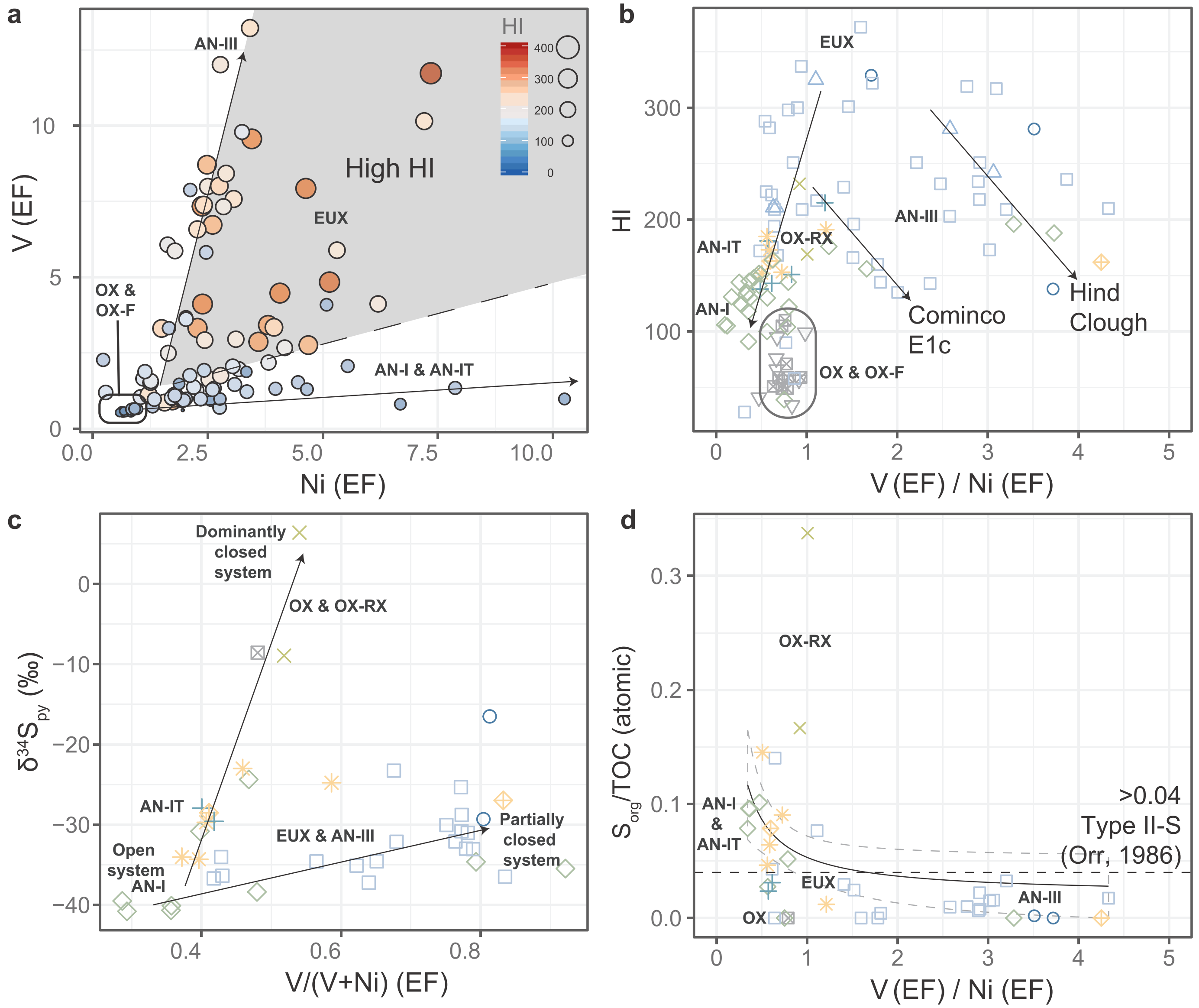

Fig. 10. Integrated organic and inorganic geochemistry. a) V versus Ni enrichment factors (EFs) with each data point scaled to hydrogen index (HI). b) HI versus V/Ni (EFs) plotted with sedimentary facies. c) Extracted pyrite stable S isotope analyses ($\delta^{34}S_{py}$) versus V/(V + Ni) using enrichment factors (EFs), plotted with sedimentary facies and approximate positions of each redox zone. See Discussion for explanation of closed versus open system conditions. d) The ratio of organic S (S_{org}) to total organic carbon (TOC) versus V/Ni (EFs), plotted with sedimentary facies and Type II-S field from Orr (1986) and with fitted regression with 2σ confidence ellipse. All plots include the approximate positions of each redox zone. See Fig. 4a for sedimentary facies key.

porosity (i.e., early diagenetic) in adjacent Facies B mudstones (see Appendix F; Emmings et al., 2019a) suggests porewater $\delta^{18}O_w$ composition was closer to −4.3‰ VSMOW. Taken together, this favours carbonate precipitation close to the sediment-seawater interface and likely under conditions dominated by sulphate reduction, near or within the sulphate-methane transition zone (e.g., Claypool and Kaplan, 1974; Scotchman, 1989; Krajewski et al., 2001; Malinverno and Pohlman, 2011; Meister, 2013). Porewater supersaturation of key metals (Ca, Mg) and high alkalinity were additional requirements for precipitation of Facies A limestones (e.g., Braissant et al., 2003; Mercedes-Martín et al., 2016). Such high alkalinity is linked to shallow AMO (Moore et al., 2004). Thus Facies A limestones are possibly analogous to modern deep-water authigenic carbonate ‘slabs’ associated with diffuse methane seeps in the Black Sea (Mazzini et al., 2004; Yurchenko, 2014). This is distinct from relatively late diagenetic carbonate-filled fractures in the Bowland Shale (Clarke et al., 2018).

Since sulphate-reducing bacteria are typically more competitive than methanogens (e.g., Burdige, 2006), relatively early onset of methanogenic conditions suggests sulphate and/or labile OM required for sulphate-reducing bacteria was rapidly exhausted near seabed. Perhaps this was driven by a high rate of OM flux into the bottom-waters, coupled with a high mean sediment accumulation rate (Emmings et al., 2019a) (Fig. 1b). Once a vigorous (i.e., near seabed) AMO front was established, it is likely that sulphate was further exhausted via sulphate-reduction coupled to AMO (Milucka et al., 2012). Thus $\delta^{34}S_{py}$ values closer to −30‰ and presence of fine pyrite euhedra in Zone EUX, compared to Zones AN-III and AN-I (Fig. 10a; Table 1), is interpreted to indicate exceptionally fast exhaustion of porewater sulphate during transition into the zone of methanogenesis.

An elevated thermocline during periods of high sea level likely promoted widespread dysoxia on shelves (e.g., Tyson and Pearson, 1991). Trace element enrichment in Namurian marine bands on shelves (Spears and Amin, 1981) suggests shelfal bottom-waters were also at least partially euxinic during periods of high sea level (Fig. 11a). Superestuarine stratification (Algeo et al., 2008) is a possible mechanism for euxinia in this setting. Assuming anoxic to euxinic conditions

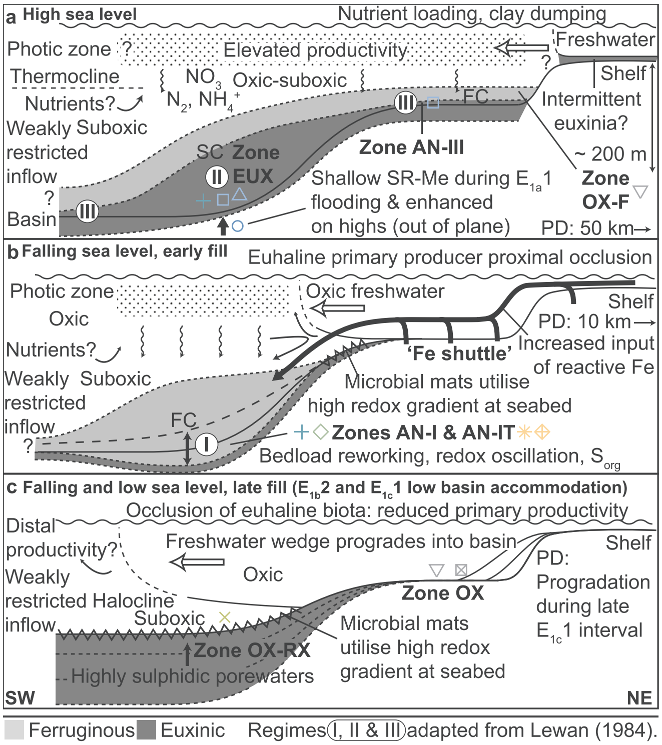

Fig. 11. Proposed models for anoxia in the Craven Basin during deposition of the Upper Bowland Shale, after Emmings et al. (2019b), during sea level maximum flooding and highstands (a), falling sea level during early basin fill (b), and falling and low sea level during late basin fill (c). Regimes I-III are adaptations of the V–Ni regimes defined by Lewan (1984). See Discussion for further details. SC = Stable chemocline (positioned permanently in the water column). FC = Fluctuating chemocline. SR-Me = sulphate reduction-methanogenesis transition zone. PD = Pendle delta system. S_{org} = Organic S. S_{sul} = solid sulphate precipitation. See Fig. 4a for sedimentary facies key.

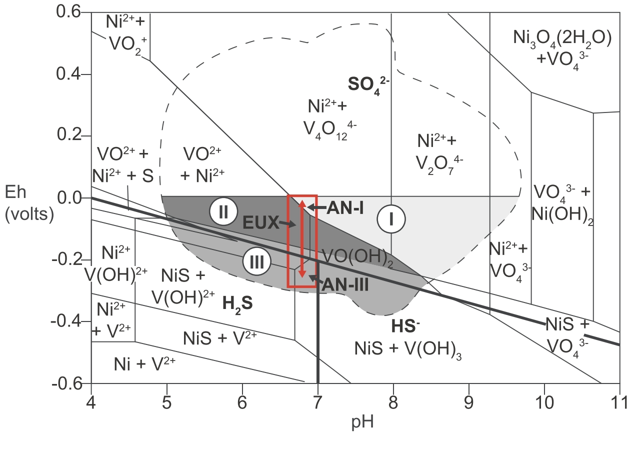

Fig. 12. Eh-pH diagram for V and Ni species and sulphide ions at expected bottom water concentrations, 25 °C and 1 ATM, redrawn from Lewan (1984) ©1984, with permission from Elsevier. The dashed outline represents the natural stability field for marginal and open marine sediments (see Lewan, 1984 and references therein). The shaded areas delineate N–Ni Regimes I, II and III, as defined by Lewan (1984). The likely ranges of zones EUX, AN-III and AN-I at expected bottom and/or porewater Eh and pH are also indicated.

extended onto shelves, Fe_{HR} was mostly fixed in bottom-waters as sulphide. This effectively immobilised a pool of Fe_{HR}, triggering synchronous basinal Fe-limitation. This mechanism may explain why marine bands generally record more sulphidic conditions (Figs. 6–7), although a higher rate of input of labile OM (therefore increased rates of sulphide production) could also explain this feature. Consistent *n*-alkane composition across zones EUX, AN-III and AN-I (Fig. 4e) suggest the type of input OM did not change significantly during deposition across these redox zones. It is therefore unlikely that euxinia was triggered by input of a radically different type of OM.

5.4. *Zone AN-III: fluctuating chemocline*

Falling sea level and/or uplift of adjacent shelves displaced the shelfal, sulphidic sink for Fe_{HR} with ferruginous anoxic, suboxic and ultimately oxic conditions. This switch probably remobilized a fraction of previously sequestered Fe_{HR} in shelfal sediments, enhancing the 'Fe shuttle' (Lyons and Severmann, 2006) into the basin during periods of lower sea level (Fig. 11b). The relatively low and highly variable Fe_{py}/Fe_{HR} record in Zone AN-III (Fig. 7c) is consistent with enhanced Fe-oxyhydroxide input to seabed and reduced precipitation of Fe-sulphide in bottom-waters. Fluctuation in the position of the water column chemocline activated the 'particulate shuttle', enhancing Mo enrichment compared to U (Figs. 3 and 6c; Algeo and Tribovillard, 2009; Emmings et al., 2019b). Increased Fe_{HR} input promoted fluctuation in the position of the water column chemocline separating ferruginous and sulphidic conditions, whilst sediment porewaters remained highly sulphidic.

Negative Eh and limited production of acids in Zone AN-III shallow sediment porewaters ensured V, Se and Cr remained competitive for fixation compared to Ni (Fig. 12), and to a lesser degree Pb, Co and As, which were likely largely recycled back into the water column. The V shuttle was possibly also larger compared to Ni under the intermittently non-sulphidic (bottom-water) conditions (Algeo and Maynard, 2004; Calvert and Pedersen, 1993).

5.5. *Zone AN-I: early diagenetic redox oscillation*

The transition from Zone AN-III to Zone AN-I is associated with a distinctive switch in enrichment between V, Se and Cr, and Ni, Pb, Co and As, respectively (compare Fig. 5c, e). For V and Ni this relationship is highly competitive and is bimodal (Fig. 10a). Zone AN-III porewaters were probably analogous to Regime III of Lewan (1984), whereas Zone AN-I porewaters were comparable to Regime I. This switch was driven by changing pH and/or Eh in porewaters during falling sea level linked to increasing supply of Fe_{HR} as a buffer for sulphide (Fig. 12).

Continued falling sea level and sustained Fe_{HR} supply to the basin sufficiently buffered sulphide so that ferruginous conditions intermittently intersected the seabed during deposition of Zone AN-I. A lower sulphate concentration in Mississippian marine seawater compared to present day (Algeo et al., 2015; Horita et al., 2002) and/or increasing proximity to freshwater supplied from the Pendle delta, potentially promoted expansion of ferruginous conditions. A large flux of Mn–Fe-oxyhydroxides is consistent with continued 'particulate shuttle' conditions (Fig. 6d). Together with evidence of enhanced physical reworking during deposition of Facies F lenticular mudstones (Emmings et al., 2019a), this process triggered redox oscillation between zones of sulphate and Fe reduction (e.g., Aller, 1998).

Zone AN-I sediments were analogous to a partially fluidised bed reactor (e.g., Aller, 1998), associated with intense sediment reworking and high frequency redox oscillation between zones of Fe and sulphate reduction. Free sulphide was strongly buffered by Fe_{HR} and porewaters were likely acidic (e.g., Li and Schieber, 2015). Zone AN-I porewaters were sufficiently acidic to completely dissolve primary carbonate (Fig. 9c), despite the presence of moulds of body fossils. Redox oscillation promotes carbonate dissolution due to long-lived and slow rates of sulphate reduction (Meister, 2013; Soetaert et al., 2007) and/or directly via the oxidation of H_2S or solid sulphides (e.g., pyrite) to produce sulphuric acid (Aller, 1982; Ku et al., 1999). Presence of the aragonite polymorph, such as ammonoid tests (e.g., Flügel, 2004), potentially enhanced this process. Presence of sulphate-bearing laminae in

Facies F (Emmings et al., 2019a) suggests pyrite oxidants, such as Mn^{4+}, Fe^{3+} and Mn^{3+} (Aller and Rude, 1988), were intermittently available and promoted local gypsum/anhydrite (i.e., S_{sul}) precipitation (Blanchet et al., 2012; Pirlet et al., 2010). Fe^{3+} liberated from pyrite oxidation was likely fixed as Fe_{ox}, migrated into high alkalinity microenvironments that promoted Fe_{carb} precipitation, or was reduced and formed secondary pyrite. This is consistent with presence of multiple pyrite forms (microcrystalline, euhedra, framboids) in Zone AN-I (Fig. 8c). $Fe_{py}/Fe_T > 0.7$ in Zone AN-I mudstones suggests bottom-waters were intermittently euxinic (Fig. 7d). However, if Fe sourced from pyrite oxidation locally migrated through porewaters, and subsequently reacted with sulphide, this is a mechanism to locally and diagenetically enrich Fe_{py}/Fe_{HR}.

During redox oscillation, trace elements Mo, Ni, As, Pb and Co, together with S, initially fixed by sulphide, were probably recycled within porewaters multiple times, prior to fixation primarily in pyrite. Emmings et al. (2019b) suggested S cycling within porewaters, and generation of reactive intermediate S species, was a key mechanism for sulphurization (Type II-S) and relatively low $\delta^{34}S_{py}$ (i.e., close to −40‰) in Zone AN-I (Fig. 9d; 10c). A relatively high Fe_{mag} content in Zone AN-I (Appendix D) also suggests the concentration of porewater sulphide was not sufficiently high to dissolve Fe_{mag} (Canfield and Berner, 1987).

V, Se and Cr, plus P, Zn and Ba (Fig. 5e), hosted primarily by solid-sulphides, phosphate, carbonate or possibly authigenic clay minerals, remained unfixed during Zone AN-I early diagenesis, due to unsuitable porewater pH, Eh, cation saturation and/or uncompetitive oxidation state associated with redox oscillation. These elements were likely recycled back into the water column or migrated into adjacent carbonate-rich packages. This effect was particularly influential on V fixation, which under moderate to high (less negative) Eh (Fig. 12), is outcompeted by Ni (Fig. 10a) for metalation in porphyrins (Lewan, 1984). V enrichment despite a lack of carbonate and phosphate in the 'transitional' AN-III package above the $E_{1a}1$ marine band at Hind Clough (Fig. 3a) demonstrates porphyrins were likely an important host for V.

5.6. Zones OX-RX, OX-F and OX: bottom water ventilation

Gradual advance of the Pendle delta from the north promoted at least partial desalination in the Craven Basin (from the $E_{1b}2$ marine band onwards; Emmings et al., 2019a). This is supported by TOC/S > 10 in Facies H–I at Cominco S9, suggesting fresh or brackish water conditions (Berner and Raiswell, 1984). Facies H–I exhibit an average Sr/Ba of ~0.4 (± 0.1 2σ), suggesting dominantly brackish conditions (Wei and Algeo, 2019). An extended or thickened freshwater lid potentially occluded euhaline macrofauna and euhaline plankton from the euphotic zone and therefore substantially reduced the export of OM to the seabed (Emmings et al., 2019b). Productivity shutdown decreased the rate of OM consumption in bottom-waters and gradually promoted bottom-water oxygenation as zones OX-RX, OX-F and OX.

Zone OX-RX represents the first period of sustained bottom-water ventilation (Fig. 11c), triggering development of oxic and/or suboxic conditions, on the basis of absence of enrichment in most redox-sensitive elements (Figs. 5b and 6f) and Fe_{HR}/Fe_T close to 0.38 (Fig. 7f). Porewaters near or at seabed were likely highly sulphidic, on the basis of marginal and selective enrichment in redox-sensitive trace elements (Figs. 5b and 6f) and pervasive pyritisation of burrows (Emmings et al., 2019a). High $\delta^{34}S_{py}$ (Fig. 10c), presence of early diagenetic pyrite nodules (Fig. 8e) and lack of Fe_{mag} (Emmings et al., 2019a, 2019b) suggests sulphidic porewater conditions in a closed system (Canfield and Berner, 1987; Canfield et al., 1992). A lack of carbonate in Zone OX-RX (Figs. 3 and 9c) suggests porewaters were also highly acidic, perhaps also associated with the oxidation of sulphide near or at the seabed, similar to Zone AN-I. Emmings et al. (2019b) suggested cycling of reactive S species across the high redox gradient near the seabed (e.g., Aplin and Macquaker, 1993) may also explain fixation of S_{org} (Type II-S) in Zone OX-RX. This was associated with the expansion of microbial mats (Emmings et al., 2019a,b), as sulphide-oxidisers (e.g., Grunke et al., 2011).

Enrichment in U in Zone OX-RX (Figs. 5b and 6f) supports the interpretation that U is fixed primarily in porewaters (e.g., Tribovillard et al., 2006). Marginal enrichment in As, Sb, Se, Cu, V and Pb (Figs. 3 and 5b) suggests these elements are fixed primarily within porewaters (rather than bottom-waters), migrated together with upward-diffusing sulphide, or were shuttled to bottom-waters under suboxic conditions. Similarly, marginal enrichment in As and Pb in Zone OX-F compared to Zone OX (Figs. 2 and 5d) suggests these elements responded to ferruginous water column conditions, and were likely shuttled to the seabed with Fe–Mn-oxyhydroxides (e.g., Tribovillard et al., 2006). This is consistent with $Fe_{HR}/Fe_T > 0.38$ in Zone OX-F (Fig. 7g). High $\delta^{34}S_{py}$ (Fig. 10c) and presence of aggregated and rare, isolated pyrite euhedra (Fig. 8f) in Zones OX-F and OX is consistent with relatively late diagenetic precipitation. Absence of enrichment in all redox-sensitive elements (Figs. 5f and 6h), presence of bioturbation (Emmings et al., 2019a) and $Fe_{HR}/Fe_{py} < 0.38$ (Fig. 7h) in Zone OX suggests deposition under non-sulphidic and at least intermittently oxygenated bottom-waters.

5.7. Synthesis

Fig. 13 delineates the seven syngenetic and early diagenetic redox zones as a function of basin evolution ($E_{1a}1$ to $E_{1c}1$ marine bands) and depth above and below seabed (~cm to m; e.g., Mossmann et al., 1991). Whilst diagenetic reactions will ultimately favour terminal electron acceptors with the highest free energy gained (Emerson and Hedges, 2004; Mazzullo, 2000), diagenetic systems are highly complex. Fig. 13 is a simplification, and assumes closed-system and low permeability conditions dominated following early diagenesis.

Preservation of HI and carbonate, in this system, was a function of changing bottom and pore water redox processes. Marine transgressions and maximum flooding surfaces (Posamentier et al., 1988), attributed to Zone EUX, exhibit high HI because OM remineralisation within sediment pores was limited to a single, and probably short-lived, period of sulphate-reduction prior to burial into the zone of methanogenesis (Fig. 13). Similarly these packages are carbonate-rich because acidity generated during early diagenesis was sufficiently buffered by primary carbonate. This robust buffering capacity was likely a result of increased input of primary carbonate and reduced supply of Fe_{HR}. Increased supply of Fe_{HR} towards the end of sea level highstands (Zone AN-III), sea level fall (Zone AN-I) and low sea level (mostly Zone AN-IT) promoted redoxcline instability and ultimately redox oscillation in porewaters. This process enhanced remineralisation of OM, therefore reducing HI, and generated considerable acidity that completely dissolved primary carbonate. During deposition of Zone AN-III, the sulphate-methane transition zone probably expanded, prior to becoming compressed and deeper during deposition of AN-I (Fig. 13).

Proximity to sources of freshwater input promoted bottom-water ventilation and development of OX-RX, OX-F and OX packages dominated by terrestrial OM. It is likely the freshwater conditions recorded in Cominco S9 indicate freshwater input local to the Pendle delta, rather than basin-wide desalination (Emmings et al., 2019a). TOC/S < 10 in contemporaneous mudstones in the Widmerpool Gulf (Gross et al., 2015), suggests marine conditions persisted in areas distal to the Pendle delta.

Early diagenetic redoxclines were capable of migration through the shallow sediment column relatively quickly, in response to sea level fluctuation, at a frequency of ~133 ka (Waters and Condon, 2012). This implies that the redoxclines between Fe and sulphate reduction, and the upper boundary of sulphate-methane transition zone, were positioned within decimetres (i.e., 10 s cm) of seabed. This is consistent with modern observations that suggest the majority of sulphate reduction proceeds within this shallow zone (Jorgensen, 1982).

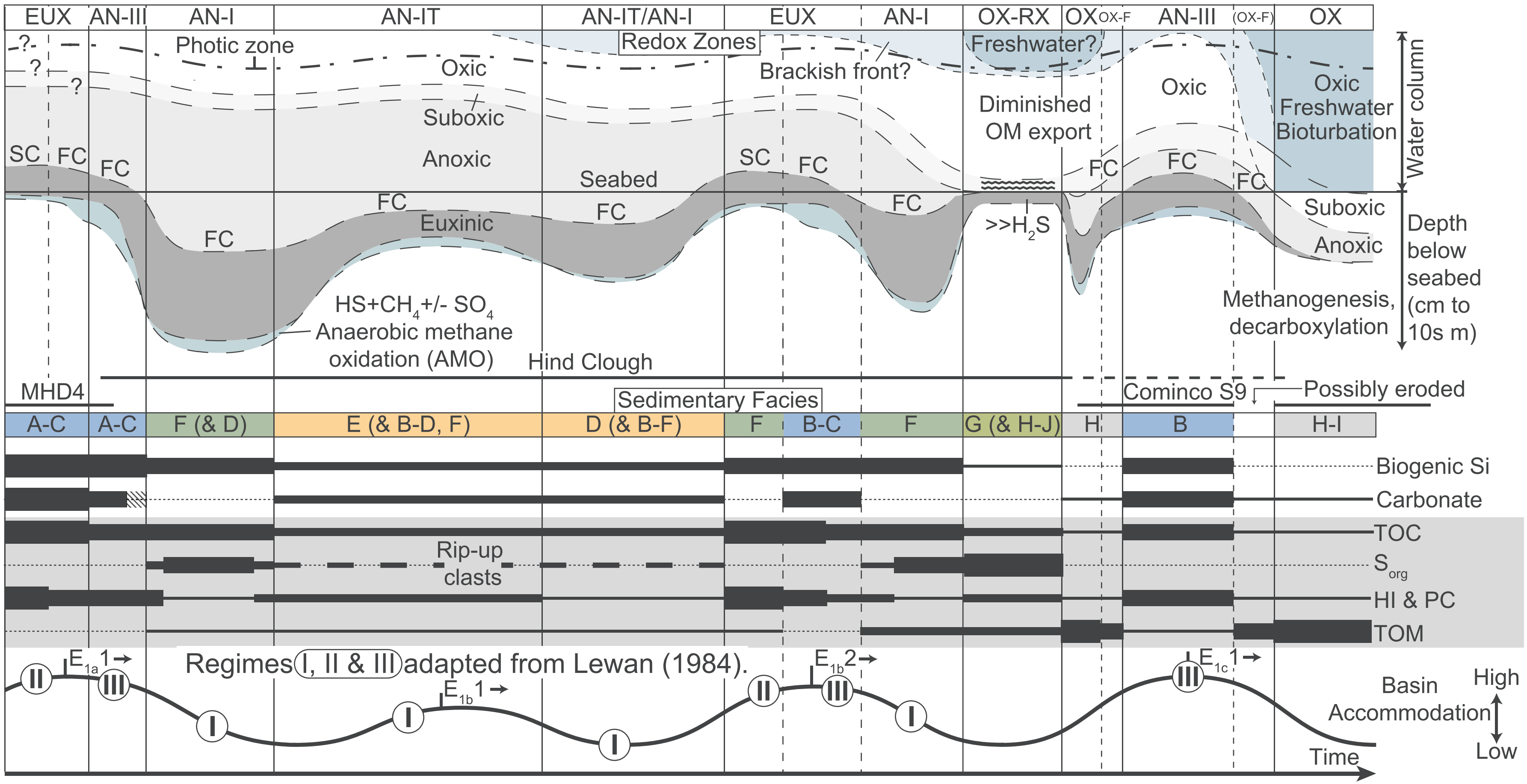

Fig. 13. Schematic for the temporal distribution of syngenetic and early diagenetic conditions through the Upper Bowland Shale in the Craven Basin, based on integration of inorganic and organic geochemical data (this study), palynology and organic S (S_{org}) analysis (Emmings et al., 2019b) and sedimentology (Emmings et al., 2019a). Time is plotted along the y-axis, from beneath the $E_{1a}1$ marine band to deposition of the Pendle Grit ($E_{1c}1$ biozone, Pendleton Formation) overlying the Bowland Shale. The magnitude of basin accommodation change is based on the areal extent of marine bands (see Waters and Condon, 2012). This is a simplification of syngenetic and diagenetic processes, designed to illustrate broadly the types of processes that operated during basin infill. Depth below seafloor is highly uncertain and variable, likely ranging from several cm to m depending on sedimentary facies, the flux of labile organic matter (OM) and bottom water geochemistry. SC = stable chemocline. FC = fluctuating chemocline. TOC = total organic carbon. S_{org} = organic sulphur. HI = hydrogen index. PC = pyrolised C. TOM = terrestrial OM. The cross-hatched interval on the carbonate panel indicates the $E_{1a}1$ ‘transitional’ interval between zones AN-III and AN-I (see Discussion). This is possibly explained by downward diffusion of acids generated during deposition of the overlying AN-I package.

Preservation of syngenetic and early diagenetic geochemical signals demonstrates significant resistance to overprint by early diagenetic oxidative 'burn-down' (*sensu* Cowie et al., 1995; Prahl et al., 2003) and late diagenetic processes. An exception is the 'transitional' AN-III interval overlying the $E_{1a}1$ marine band, which exhibits enrichment in trace elements associated with low porewater Eh and yet lacks carbonate (Fig. 3a). This is possibly explained by downward diffusion of acids generated during deposition of the overlying AN-I package. Siderite and sulphate nodules above the base of the $E_{1b}2$ marine band (Emmings et al., 2019a) were also potentially formed in response to rapid deepening of oxidation fronts during deposition of the overlying zones AN-I and/or OX-RX (Fig. 13).

Resistance to late diagenetic alteration is consistent with the interpretation that sulphides host many redox-sensitive trace elements (Tribovillard et al., 2006). Thermal maturation of OM can promote migration of trace metals, such as V and Ni, into bitumen (Filby, 1994; Lewan, 1984). The low thermal maturity of the studied sites (Fig. 4a) precludes full assessment of the effect of late diagenetic processes. However, at least to the 'oil window' (~60 °C; Tissot and Welte, 1984), sediments were apparently 'locked-in' to a consistent and uniform diagenetic pathway and with minimal evidence for pore fluids permeating across early diagenetic redox zones (i.e., veins are rare; Emmings et al., 2019a).

5.8. Implications for hydrocarbon and mineral systems

Sedimentary delivery mechanism imparts an important diluting or concentrating effect on TOC. Thus TOC tends to be lower in sediment density flow deposits (Facies D-E; Figs. 2–3, 4c). Phases of increased (OM-lean) mud clast supply during deposition of Facies F also likely promoted dilution of TOC. Similarly, periods of high sea level were potentially associated with higher rates of primary productivity and therefore OM export to bottom-waters. Autodilution (e.g., by radiolaria) was also likely an important control on TOC during periods of high euphotic zone productivity. Buried OM was then subject to partial consumption and repackaging as part of the anoxic food web (e.g., Burdige, 2006).

Pores that develop within oil-prone (i.e., Type I or II) OM are possibly an important variable for understanding shale gas prospectivity (e.g., Jarvie et al., 2007; Loucks et al., 2009) with periods of enhanced preservation of Type I or II particulate OM more likely to be relatively prospective. Productive water column conditions and Fe-limitation during periods of high sea level (i.e., marine bands, zones EUX and AN-III) promoted the concentration and/or preservation of Type I or II OM. Marine bands, particularly on basinal highs (e.g., MHD4; Fig. 3b), are likely to be the most suitable intervals in terms of organic pore development during catagenesis. Marine bands are also likely considered prospective due to pervasive carbonate and silica cements (Passey et al., 2010). S_{org} exerts an important control on hydrocarbon prospectivity, as a catalyst for early thermal maturation (e.g., Lewan, 1998) and expulsion of S, including H_2S (e.g., Aizenshtat et al., 1995). High S_{org} content is associated with periods of diagenetic redox oscillation and manifested as candidate microbial mats on the transition from anoxic to oxic bottom-waters (Fig. 13; Emmings et al., 2019b).

Palaeoredox cycles can be recognised solely using Rock-Eval pyrolysis parameters. Euxinia promoted OM preservation (Zone EUX; Fig. 9c). Porewater acidity, triggered by high Fe_{HR} loadings, promoted dissolution of primary carbonate (pathways 1 and 2; Fig. 9c). In most cases, this was associated with enhanced OM degradation, which lowered HI (zones AN-III, then AN-I; pathway 2; Fig. 9c). During and/or following carbonate dissolution, high porewater alkalinity and metal (Ca, Mg) supersaturation promoted local carbonate precipitation (mostly dolomite and/or siderite) primarily in relatively porous facies (Zone AN-IT, Facies E; pathway 3; Fig. 9c). Spherulitic limestones linked to shallow AMO plot along pathway 4 (Zone EUX; Facies A; Fig. 9c).

The distinctive switch in carbonate phases through each redox zone (pyroMINC; siderite, versus oxiMINC; calcite, dolomite) is delineated using the ratio of pyrolised inorganic C to oxidised inorganic C (Fig. 9d; *sensu* Lafargue et al., 1998; Pillot et al., 2014). Samples plot on a spectrum passing through each redox zone. Zone EUX exhibits low pyroMINC/oxiMINC and high HI because euxinic conditions promoted preservation of primary carbonate and OM. Increasing destabilisation of redoxclines through zones AN-III to AN-I(T), associated with increasing input of Fe_{HR}, is recognised by increased pyroMINC/oxiMINC and reduced HI. This is best explained by enhanced OM degradation and acid generation via redox oscillation, which dissolved primary carbonate and ultimately promoted local precipitation of Fe-carbonate phases (including dolomite and siderite). Zone OX associated with low productivity, freshwater and oxygenated conditions, is defined by samples with high pyroMINC/oxiMINC and very low HI. This is interpreted as a combination of reduced input of primary carbonate, enhanced fixation of Fe_{HR} in diagenetic carbonate under S-limited conditions (i.e., dolomite, siderite) and increased input/preservation of Type III OM.

The presence of interlocking carbonate, quartz and sulphide crystals along silt-to-sand-sized laminae and beds in Zone AN-IT (Fig. 8d) suggests these layers were a conduit for relatively late advection of metal-rich sulphidic fluids. This is supported by relatively high $\delta^{34}S_{py}$ (Fig. 10c; Table 1). This mode of mineralisation is possibly analogous to the model described by Pedersen et al. (2003). Thus redox oscillation potentially provides a mechanism for the temporary solution of key metals in porewaters, such as Zn, prior to migration into, and concentration and precipitation in, adjacent facies if sufficiently permeable.

Patterns of redox-sensitive trace element enrichment (Fig. 5), sensitive to changing pH and Eh conditions, are a potential chemostratigraphic proxy (e.g., Riley et al., 2016) that delineates bottom-water redox cyclicity. V and Ni competition (Fig. 10a; 12) was apparently particularly vigorous during deposition of the Bowland Shale. Variable V/Ni also highlights the complexities of these elements as a source rock fingerprint in oils (e.g., Filby, 1994; Gao et al., 2017). The highly competitive nature of V and Ni in this system is probably linked to the relatively high sediment accumulation rate (Fig. 1b; Emmings et al., 2019a) that promoted fixation within sediments rather than the water column. Zone EUX is associated with relatively stable euxinic conditions and is therefore an exception to this rule, perhaps due to a lower sediment accumulation rate (i.e., maximum flooding surface) and/or increased rate of sulphide production. Competition was potentially also promoted by dominance of a single host phase, such as free-base porphyrins sourced from chlorophyll (e.g., Pratt and Davis, 1992; Filby, 1994). Therefore V and Ni competition in the Bowland Shale was so pronounced perhaps because sediments received a relatively large input of chlorophyll, consistent with the interpretation of a large flux of autochthonous OM (Emmings et al., 2019b).

OM was clearly highly prone to degradation under anoxic conditions, particularly under redox oscillation conditions. This process impacted strongly on the hydrocarbon prospectivity and metal distribution through the Bowland Shale, including reduction of HI and complete dissolution of primary carbonate. Redox oscillation promoted dissolution of carbonate in shallow sediments, activating this part of the inorganic C cycle. Redox oscillation is linked to metal (incl. Fe) oxide-rich conditions, a high mean sediment accumulation rate and input of highly labile OM. The capacity for temporary storage and shuttling of reactive Fe was apparently enhanced by water-column chemocline fluctuation, in response to sea level fluctuation, within a highly complex and variable bathymetric setting. Redox oscillation is linked to an enhanced shelf-to-basin Fe shuttle, specifically during periods of falling sea level, where ventilation of shelves likely promoted re-mobilisation of reactive Fe. Therefore seaways defined by inherited block-and-basin rift structures are likely to be particularly prone to redox oscillation processes.

Input of readily hydrolysable cellular OM, likely including abundant extracellular polymeric substances (EPS), is consistent with high rates of sulphide production. Perhaps these compounds were sourced from cyanobacteria, radiolaria or another presently unresolved primary producer of the late-Palaeozoic 'Phytoplankton Blackout' (Riegel, 1996, 2008; Tappan, 1970). This suggests colonisation by labile primary producers in late-Palaeozoic epicontinental basins was a key preconditioning requirement for the development of redox oscillation in this black shale succession.

6. Conclusions

Sedimentological observations, organic and stable isotope geochemistry and palaeoredox proxies were integrated through the Upper Bowland Shale at three sites in the Craven Basin (Lancashire, UK) in order to constrain syngenetic and early diagenetic processes. Organic matter (OM) in the Upper Bowland Shale comprises a mixture of Type II, II-S, II/III and III OM. 'Redox zones' are defined by patterns of Fe-speciation and redox-sensitive trace element enrichment. Fluctuating sea level moderated the efficiency of the shelf-to-basin reactive Fe (Fe_{HR}) shuttle. This was a key control on the position and stability of redoxclines between zones of Fe and sulphate reduction, and methanogenesis. Falling sea level and increasing Fe_{HR} supply is recognised as a switch from zones EUX (transgressive and early highstand systems tracts), AN-III (late highstand systems tracts) and ultimately AN-I and AN-IT (falling stage and lowstand systems tracts).

Preservation of HI and carbonate, in this system, was a function of changing bottom and pore water redox processes. OM was highly prone to degradation under anoxic conditions, particularly under oscillatory redox conditions. Zone EUX is carbonate-rich and exhibits high HI because OM remineralisation within sediment pores was limited to a single, and probably short-lived, period of sulphate-reduction prior to transition into the zone of methanogenesis. Increased shelf-to-basin supply of Fe_{HR} during sea level fall destabilised redoxclines and ultimately triggered redox oscillation between Fe and sulphate reduction in porewaters (Zone AN-I). This process enhanced remineralisation of OM, significantly reduced HI and generated acidity that completely dissolved primary carbonate. Redox oscillation is linked to the following conditions; input of OM prone to degradation under anoxic conditions; weak basin restriction; metal-rich conditions; a relatively high 'pro-deltaic' mean sediment accumulation rate; high-frequency sea level fluctuation; and a complex bathymetric setting. These findings are important for understanding ancient biogeochemical cycles and Late Palaeozoic black shales in the context of hydrocarbon and metal systems.

Data availability

All supporting data and method statements are provided in the accompanying supplementary files. The dataset is also available via the National Geoscience Data Centre (NGDC) open-access repository (Emmings et al., 2019c) [https://dx.doi.org/10.5285/c14ed206-bc46-4f61-938b-171b16205c44].

Declaration of competing interest

The authors declare that they have no known competing financial interests or personal relationships that could have appeared to influence the work reported in this paper.

Acknowledgments

This study was funded by the Natural Environment Research Council (NERC) [including grant no. NE/L002493/1, within the Central England Training Alliance (CENTA)]. The study also received CASE funding from the British Geological Survey. *n*-alkane biomarkers were part-funded by the AAPG Foundation Donald F. Towse Memorial Grant 2016. SWP acknowledges support from a Royal Society Wolfson Research Merit Award and a Leverhulme Research Fellowship. Nick Riley (Carboniferous Ltd) is thanked for sharing biostratigraphic expertise and assistance. Nick Marsh and Tom Knott are thanked for providing assistance during geochemical analyses. Chris Kendrick is thanked for production of the organic carbon isotope data. Hilary Sloane and Jack Lacey (BGS) are thanked for production of the carbon and oxygen (carbonate) isotope data. Pete Sadler (University of California) is thanked for compilation and provision of the background sediment accumulation rate dataset. We gratefully acknowledge the valuable comments by Nicolas Tribovillard and an anonymous reviewer which helped shape this paper. Published with permission of the Director of the British Geological Survey.

Appendix A. Supplementary data

Supplementary data to this article can be found online at https://doi.org/10.1016/j.palaeo.2019.109423.

References

Aitkenhead, N., Bridge, D., Riley, N.J., Kimbell, S., 1992. Geology of the Country Around Garstang: Memoir for 1:50 000 Sheet 67. HMSO, London.

Aizenshtat, Z., Krein, E.B., Vairavamurthy, M.A., Goldstein, T.P., 1995. Role of sulfur in the transformations of sedimentary organic matter: a mechanistic overview, geochemical transformations of sedimentary sulfur. In: ACS Symposium Series. American Chemical Society, pp. 16–37.

Algeo, T., Heckel, P.H., Maynard, J.B., Blakey, R., Rowe, H., 2008. Modern and ancient epeiric seas and the super-estuarine circulation model of marine anoxia. In: Pratt, Holmden (Ed.), Special Paper 48: Dynamics of Epeiric Seas, pp. 7–38.

Algeo, T.J., Tribovillard, N., 2009. Environmental analysis of paleoceanographic systems based on molybdenum–uranium covariation. Chemical Geology 268 (3–4), 211–225.

Algeo, T.J., Luo, G.M., Song, H.Y., Lyons, T.W., Canfield, D.E., 2015. Reconstruction of secular variation in seawater sulfate concentrations. Biogeosciences 12 (7), 2131–2151.

Algeo, T.J., Lyons, T.W., 2006. Mo–total organic carbon covariation in modern anoxic marine environments: implications for analysis of paleoredox and paleohydrographic conditions. Paleoceanography 21 (1) n/a-n/a.

Algeo, T.J., Maynard, J.B., 2004. Trace-element behavior and redox facies in core shales of Upper Pennsylvanian Kansas-type cyclothems. Chem. Geol. 206 (3–4), 289–318.

Aller, R.C., 1982. Carbonate dissolution in nearshore terrigenous muds: the role of physical and biological reworking. J. Geol. 90 (1), 79–95.

Aller, R.C., 1994. Bioturbation and remineralization of sedimentary organic matter: effects of redox oscillation. Chem. Geol. 114 (3), 331–345.

Aller, R.C., 1998. Mobile deltaic and continental shelf muds as suboxic, fluidized bed reactors. Mar. Chem. 61 (3), 143–155.

Aller, R.C., Rude, P.D., 1988. Complete oxidation of solid phase sulfides by manganese and bacteria in anoxic marine sediments. Geochem. Cosmochim. Acta 52 (3), 751–765.

Alvera-Azcárate, A., et al., 2011. Thermocline characterisation in the Cariaco basin: a modelling study of the thermocline annual variation and its relation with winds and chlorophyll-a concentration. Cont. Shelf Res. 31 (1), 73–84.

Andrews, I.J., 2013. The Carboniferous Bowland Shale Gas Study: Geology and Resource Estimation. British Geological Survey for Department of Energy and Climate Change.

Aplin, A.C., Macquaker, J.H.S., 1993. Quantifying sedimentary geochemical processes - C-S-Fe geochemistry of some modern and ancient anoxic marine muds and mudstones. Philos. Trans. R. Soc. London, Ser. A: Phys. Eng. Sci. 344 (1670), 89–100.

Arthurton, R.S., 1972. Record of Shaft or Borehole. Institute of Geological Sciences, Cominco S9.

Arthurton, R.S., 1984. The Ribblesdale fold belt, NW England—a Dinantian-early Namurian dextral shear zone. Geological Society, London, Special Publications 14 (1), 131–138.

Ashton, J.H., et al., 2016. The Giant Navan carbonate-hosted Zn–Pb deposit: exploration and geology: 1970–2015. Appl. Earth Sci. 125 (2), 75–76.

Bennett, R.H., et al., 1999. Early diagenesis: impact of organic matter on mass physical properties and processes, California continental margin. Mar. Geol. 159 (1), 7–34.

Berner, R.A., Raiswell, R., 1984. C/S method for distinguishing freshwater from marine sedimentary rocks. Geology 12 (6), 365–368.

Bianchi, T.S., 2011. The role of terrestrially derived organic carbon in the coastal ocean: a changing paradigm and the priming effect. Proc. Natl. Acad. Sci. U. S. A 108 (49), 19473–19481.

Bijkerk, J.F., 2014. External Controls on Sedimentary Sequences: a Field and Analogue Modelling-Based Study.

Bisat, W.S., 1923. The carboniferous goniatites of the north of England and their zones. Proc. Yorks. Geol. Soc. 20 (1), 40–124.

Blanchet, C.L., et al., 2012. Influence of diagenesis on the stable isotopic composition of biogenic carbonates from the Gulf of Tehuantepec oxygen minimum zone. Geochem. Geophys. Geosyst. 13 (4).

Bourbonniere, R.A., Meyers, P.A., 1996. Sedimentary geolipid records of historical changes in the watersheds and productivities of Lakes Ontario and Erie. Limnol. Oceanogr. 41 (2), 352–359.

Braissant, O., Cailleau, G., Dupraz, C., Verrecchia, E.P., 2003. Bacterially induced mineralization of calcium carbonate in terrestrial environments: the role of exopolysaccharides and amino acids. J. Sediment. Res. 73 (3), 485–490.

Brandon, A., et al., 1998. Geology of the Country Around Lancaster: Memoir for 1:50 000 Sheet 59. The Stationary Office, London.

Bu, H., et al., 2017. Effects of complexation between organic matter (OM) and clay mineral on OM pyrolysis. Geochem. Cosmochim. Acta 212 (Suppl. C), 1–15.

Burdige, D.J., 2006. Geochemistry of Marine Sediments. Princeton University Press, USA.

Burdige, D.J., 2007. Preservation of organic matter in marine Sediments: controls, mechanisms, and an imbalance in sediment organic carbon budgets? Chem. Rev. 107 (2), 467–485.

Calvert, S.E., Pedersen, T.F., 1993. Geochemistry of Recent oxic and anoxic marine sediments: implications for the geological record. Mar. Geol. 113 (1), 67–88.

Canfield, D.E., 1994. Factors influencing organic carbon preservation in marine sediments. Chem. Geol. 114 (3), 315–329.

Canfield, D.E., Berner, R.A., 1987. Dissolution and pyritization of magnetite in anoxic marine sediments. Geochem. Cosmochim. Acta 51 (3), 645–659.

Canfield, D.E., Farquhar, J., Zerkle, A.L., 2010. High isotope fractionations during sulfate reduction in a low-sulfate euxinic ocean analog. Geology 38 (5), 415–418.

Canfield, D.E., Raiswell, R., Bottrell, S.H., 1992. The reactivity of sedimentary iron minerals toward sulfide. Am. J. Sci. 292 (9), 659–683.

Canfield, D.E., Raiswell, R., Westrich, J.T., Reaves, C.M., Berner, R.A., 1986. The use of chromium reduction in the analysis of reduced inorganic sulfur in sediments and shales. Chem. Geol. 54 (1), 149–155.

Canfield, D.E., Teske, A., 1996. Late Proterozoic rise in atmospheric oxygen concentration inferred from phylogenetic and sulphur-isotope studies. Nature 382, 127.

Casey, R., 1993. Radiolaria. In: Lipps, J. (Ed.), Fossil Prokaryotes and Protists, Boston, Massachusetts, pp. 249–284.

Chambers, L.A., Trudinger, P.A., Smith, J.W., Burns, M.S., 1975. Fractionation of sulfur isotopes by continuous cultures of Desulfovibrio desulfuricans. Can. J. Microbiol. 21 (10), 1602–1607.

Church, K.D., Gawthorpe, R.L., 1994. High resolution sequence stratigraphy of the late namurian in the Widmerpool Gulf (east midlands, UK). Mar. Pet. Geol. 11 (5), 528–544.

Clarke, H., Turner, P., Bustin, R.M., Riley, N., Besly, B., 2018. Shale gas resources of the Bowland Basin, NW England: a holistic study. Pet. Geosci. 24 (3), 287–322.

Claypool, G.E., Kaplan, I.R., 1974. The origin and distribution of methane in marine sediments. In: Kaplan, I.R. (Ed.), Natural Gases in Marine Sediments. Springer US, Boston, MA, pp. 99–139.

Cowie, G., Hedges, J.I., Prahl, F., de Lange, G., 1995. Elemental and major biochemical changes across an oxidation front in a relict turbidite: an oxygen effect. Geochem. Cosmochim. Acta 59 (1), 33–46.

Curtis, C.D., 1977. Geochemistry: sedimentary geochemistry: environments and processes dominated by involvement of an aqueous phase. Philos. Trans. R. Soc. Lond. Ser. A Math. Phys. Sci. 286 (1336), 353–372.

Davies, R.J., Austin, R., Moore, D., 1993. Environmental Controls of Brigantian Conodont-Distribution: Evidence from the Gayle Limestone of the Yoredale Group in Northern England. vol. 116. Annales de la Société géologique de Belgique, pp. 221–241 Fascicule 2 - Carboniferous biostratigraphy.

Davies, S.J., 2008. The record of Carboniferous sea-level change in low-latitude sedimentary successions from Britain and Ireland during the onset of the late Paleozoic ice age. Geol. Soc. Am. Spec. Pap. 441, 187–204.

Davydov, V.I., Crowley, J.L., Schmitz, M.D., Poletaev, V.I., 2010. High-precision U-Pb zircon age calibration of the global Carboniferous time scale and Milankovitch band cyclicity in the Donets Basin, eastern Ukraine. Geochem. Geophys. Geosyst. 11 (1), 1–22.

Davydov, V.I., Korn, D., Schmitz, M., 2012. The Carboniferous Period. Geologic Time Scale 2012 2-Volume Set. Elsevier.

Earp, J.R., 1961. Geology of the Country Around Clitheroe and Nelson (One-inch Geological Sheet 68, New Series). H.M.S.O.

Emerson, S., Hedges, J., 2004. Sediment diagenesis and benthic flux. In: Turekian, K.K., Holland, H.D. (Eds.), Treatise on Geochemistry. Elsevier, Amsterdam, pp. 293–320.

Emmings, J., 2018. Controls on UK Lower Namurian Shale Gas Prospectivity: Understanding the Spatial and Temporal Distribution of Organic Matter in Siliciclastic Mudstones. University of Leicester PhD Thesis.

Emmings, J.F., Davies, S., Vane, C.H., Moss-Hayes, V., Stephenson, M., 2019a. From Marine Bands to Hybrid Flows: Sedimentology of a Mississippian Black Shale. Sedimentology (in press).

Emmings, J.F., et al., 2019b. Controls on amorphous organic matter type and sulphurization in a Mississippian black shale. Rev. Palaeobot. Palynol. 268, 1–18.

Emmings, J.F., et al., 2019c. Data accompanying: Emmings et al. A Mississippian Black Shale Record of Redox Oscillation. Palaeogeogr. Palaeoclimatol. Palaeoecol [submitted July 2019]. National Geoscience Data Centre, British Geological Survey.

Erickson, B.E., Helz, G.R., 2000. Molybdenum(VI) speciation in sulfidic waters:: stability and lability of thiomolybdates. Geochem. Cosmochim. Acta 64 (7), 1149–1158.

Espitalie, J., Madec, M., Tissot, B., 1980. Role of mineral matrix in kerogen pyrolysis: influence on petroleum generation and migration. Am. Assoc. Petrol. Geol. Bull. 59–66.

Espitalie, J., Madec, M., Tissot, B., Mennig, J.J., Leplat, P., 1977. Source rock characterization method for petroleum exploration. In: Offshore Technology Conference.

Fenchel, T., King, G.M., Blackburn, T.H., 2012. Bacterial Biogeochemistry. In: The Ecophysiology of Mineral Cycling, third ed. Academic Press, Boston, xi-xiii.

Filby, R.H., 1994. Origin and nature of trace element species in crude oils, bitumens and kerogens: implications for correlation and other geochemical studies. Geol. Soc. Lond. Spec. Publ. 78 (1), 203–219.

Flügel, E., 2004. Microfacies of Carbonate Rocks: Analysis, Interpretation and Application. Springer Berlin Heidelberg.

Fraser, A.J., Gawthorpe, R., 2003. An Atlas of Carboniferous Basin Evolution in Northern England. Geological Society, London Memoir 28.

Fraser, A.J., Gawthorpe, R.L., 1990. Tectono-stratigraphic Development and Hydrocarbon Habitat of the Carboniferous in Northern England, vol. 55. Geological Society of London Special Publication, pp. 49–86 1.

Froelich, P.N., et al., 1979. Early oxidation of organic matter in pelagic sediments of the eastern equatorial Atlantic: suboxic diagenesis. Geochem. Cosmochim. Acta 43 (7), 1075–1090.

Ganeshram, R.S., Calvert, S.E., Pedersen, T.F., Cowie, G.L., 1999. Factors controlling the burial of organic carbon in laminated and bioturbated sediments off NW Mexico: implications for hydrocarbon preservation. Geochem. Cosmochim. Acta 63 (11), 1723–1734.

Gao, Y., Casey, J.F., Bernardo, L.M., Yang, W., Bissada, K.K., 2017. Vanadium Isotope Composition of Crude Oil: Effects of Source, Maturation and Biodegradation. Geological Society, London, Special Publications, pp. 468.

Gastaldo, R.A., Purkyňová, E., Šimůnek, Z., Schmitz, M.D., 2009. Ecological persistence in the late mississippian (serpukhovian, namurian A) megafloral record of the upper silesian basin, Czech republic. Palaios 24 (6), 336–350.

Gong, C., Hollander, D.J., 1997. Differential contribution of bacteria to sedimentary organic matter in oxic and anoxic environments, Santa Monica Basin, California. Org. Geochem. 26 (9), 545–563.

Gross, D., et al., 2015. Organic geochemistry of Mississippian shales (Bowland Shale Formation) in central Britain: implications for depositional environment, source rock and gas shale potential. Mar. Pet. Geol. 59 (0), 1–21.

Grunke, S., et al., 2011. Niche differentiation among mat-forming, sulfide-oxidizing bacteria at cold seeps of the nile deep sea fan (eastern mediterranean sea). Geobiology 9 (4), 330–348.

Habicht, K.S., Canfield, D.E., 1997. Sulfur isotope fractionation during bacterial sulfate reduction in organic-rich sediments. Geochem. Cosmochim. Acta 61 (24), 5351–5361.

Hartnett, H.E., Keil, R.G., Hedges, J.I., Devol, A.H., 1998. Influence of oxygen exposure time on organic carbon preservation in continental margin sediments. Nature 391, 572.

Hennissen, J.A.I., et al., 2017. The prospectivity of a potential shale gas play: an example from the southern Pennine Basin (central England, UK). Mar. Pet. Geol. 86, 1047–1066.

Henrichs, S.M., 1992. Early diagenesis of organic matter in marine sediments: progress and perplexity. Mar. Chem. 39 (1), 119–149.

Holdsworth, B., Collinson, J.D., 1988. Millstone Grit cyclicity revisited. In: Besly, B.M., Kelling, G. (Eds.), Sedimentation in a Synorogenic Basin Complex: the Upper Carboniferous of Northwest Europe. Blackie, Glasgow, pp. 132–152.

Horita, J., Zimmermann, H., Holland, H.D., 2002. Chemical evolution of seawater during the Phanerozoic: implications from the record of marine evaporites. Geochem. Cosmochim. Acta 66 (21), 3733–3756.

Jarvie, D.M., Hill, R.J., Ruble, T.E., Pollastro, R.M., 2007. Unconventional shale gas systems: the Mississippian Barnett Shale of north-central Texas as one model for thermogenic shale gas assessment. In: Hill, R.J., Jarvie, D.M. (Eds.), AAPG Bulletin Special Issue: Barnett Shale, pp. 475–499.

Jorgensen, B.B., 1982. Mineralization of organic matter in the sea bed -the role of sulphate reduction. Nature 296 (5858), 643–645.

Joseph, C., et al., 2013. Methane-derived authigenic carbonates from modern and paleoseeps on the Cascadia margin: mechanisms of formation and diagenetic signals. Palaeogeogr. Palaeoclimatol. Palaeoecol. 390, 52–67.

Kampschulte, A., Bruckschen, P., Strauss, H., 2001. The sulphur isotopic composition of trace sulphates in Carboniferous brachiopods: implications for coeval seawater, correlation with other geochemical cycles and isotope stratigraphy. Chem. Geol. 175 (1), 149–173.

Kane, I.A., 2010. Development and flow structures of sand injectites: the Hind Sandstone Member injectite complex, Carboniferous, UK. Mar. Pet. Geol. 27, 1200–1215.

Kaplan, I.R., Rittenberg, S.C., 1964. Microbiological fractionation of sulphur isotopes. Microbiology 34 (2), 195–212.

Keil, R.G., Mayer, L.M., 2014. 12.12 - mineral matrices and organic matter A2 - holland, heinrich D. In: Turekian, K.K. (Ed.), Treatise on Geochemistry, second ed. Elsevier, Oxford, pp. 337–359.

Kemp, A.L.W., Thode, H.G., 1968. The mechanism of the bacterial reduction of sulphate and of sulphite from isotope fractionation studies. Geochem. Cosmochim. Acta 32 (1), 71–91.

Kim, S.-T., O'Neil, J.R., 1997. Equilibrium and nonequilibrium oxygen isotope effects in synthetic carbonates. Geochem. Cosmochim. Acta 61 (16), 3461–3475.

Kirby, G.A., et al., 2000. Structure and Evolution of the Craven Basin and Adjacent Areas. Subsurface Memoir of the British Geological Survey.

Knicker, H., 2004. Stabilization of N-compounds in soil and organic-matter-rich sediments—what is the difference? Mar. Chem. 92 (1), 167–195.

Könitzer, S.F., Stephenson, M.H., Davies, S.J., Vane, C.H., Leng, M.J., 2016. Significance of sedimentary organic matter input for shale gas generation potential of Mississippian Mudstones, Widmerpool Gulf, UK. Rev. Palaeobot. Palynol. 224 (Part 2), 146–168.

Krajewski, K.P., Łącka, B., Kuźniarski, M., Orłowski, R., Prejbisz, A., 2001. Diagenetic origin of carbonate in the marhogda bed (Jurassic) in spitsbergen. Svalbard. Pol. Polar Res. 22, 89–128.

Ku, T.C.W., Walter, L.M., Coleman, M.L., Blake, R.E., Martini, A.M., 1999. Coupling between sulfur recycling and syndepositional carbonate dissolution: evidence from oxygen and sulfur isotope composition of pore water sulfate, South Florida Platform. U.S.A. Geochimica Cosmochim. Acta 63 (17), 2529–2546.

Lafargue, E., Marquis, F., Pillot, D., 1998. Rock-eval 6 applications in hydrocarbon exploration, production, and soil contamination studies. Rev. Inst. Fr. Pet. 53 (4), 421–437.

Lash, G.G., 2015. Pyritization induced by anaerobic oxidation of methane (AOM) – an example from the upper devonian shale succession, western New York, USA. Mar. Pet. Geol. 68, 520–535.

Lazar, O.R., Bohacs, K.M., Macquaker, J.H.S., Schieber, J., Demko, T.M., 2015. Capturing key attributes of fine-grained sedimentary rocks in outcrops, cores and thin sections: nomenclature and description guidelines. J. Sediment. Res. 85, 230–246.

Leeder, M.R., 1982. Upper Palaeozoic basins of the British Isles—caledonide inheritance versus Hercynian plate margin processes. J. Geol. Soc. 139 (4), 479–491.

Lewan, M.D., 1984. Factors controlling the proportionality of vanadium to nickel in crude oils. Geochem. Cosmochim. Acta 48 (11), 2231–2238.

Lewan, M.D., 1986. Stable carbon isotopes of amorphous kerogens from Phanerozoic sedimentary rocks. Geochem. Cosmochim. Acta 50 (8), 1583–1591.

Lewan, M.D., 1998. Sulphur-radical control on petroleum formation rates. Nature 391 (6663), 164–166.

Li, Y., Schieber, J., 2015. On the origin of a phosphate enriched interval in the Chattanooga Shale (Upper Devonian) of Tennessee—a combined sedimentologic, petrographic, and geochemical study. Sediment. Geol. 329, 40–61.

Loucks, R., Reed, R., Ruppel, S., Jarvie, D.M., 2009. Morphology, genesis, and distribution of nanometerscale pores in siliceous mudstones of the Mississippian Barnett Shale. J. Sediment. Res. 79, 848–861.

Loyd, S.J., et al., 2016. Methane seep carbonates yield clumped isotope signatures out of equilibrium with formation temperatures. Nat. Commun. 7, 12274.

Lyons, T.W., Severmann, S., 2006. A critical look at iron paleoredox proxies: new insights from modern euxinic marine basins. Geochem. Cosmochim. Acta 70 (23), 5698–5722.

Malinverno, A., Pohlman, J.W., 2011. Modeling sulfate reduction in methane hydrate-bearing continental margin sediments: does a sulfate-methane transition require anaerobic oxidation of methane? Geochem. Geophys. Geosyst. 12 (7).

Martinsen, O.J., Collinson, J.D., Holdsworth, B.K., 1995. Millstone Grit Cyclicity Revisited, II: Sequence Stratigraphy and Sedimentary Responses to Changes of Relative Sea-Level, Sedimentary Facies Analysis. Blackwell Publishing Ltd., pp. 305–327.

Mayer, L.M., 1994. Surface area control of organic carbon accumulation in continental shelf sediments. Geochem. Cosmochim. Acta 58 (4), 1271–1284.

Maynard, J.R., Leeder, M.R., 1992. On the periodicity and magnitude of Late Carboniferous glacio-eustatic sea-level changes. J. Geol. Soc. 149 (3), 303–311.

Mazzini, A., et al., 2004. Methane-related authigenic carbonates from the Black Sea: geochemical characterisation and relation to seeping fluids. Mar. Geol. 212 (1), 153–181.

Mazzullo, S.J., 2000. Organogenic dolomitization in peritidal to deep-sea sediments. J. Sediment. Res. 70 (1), 10–23.

McLennan, S.M., 2001. Relationships between the trace element composition of sedimentary rocks and upper continental crust. Geochemistry, Geophysics, Geosystems 2 (4). https://doi.org/10.1029/2000GC000109.

Meister, P., 2013. Two opposing effects of sulfate reduction on carbonate precipitation in normal marine, hypersaline, and alkaline environments. Geology 41 (4), 499–502.

Menning, M., et al., 2006. Global time scale and regional stratigraphic reference scales of central and west europe, east europe, tethys, south China, and north America as used in the devonian–carboniferous–permian correlation chart 2003 (DCP 2003). Palaeogeogr. Palaeoclimatol. Palaeoecol. 240 (1–2), 318–372.

Mercedes-Martín, R., et al., 2016. Growing spherulitic calcite grains in saline, hyperalkaline lakes: experimental evaluation of the effects of Mg-clays and organic acids. Sediment. Geol. 335, 93–102.

Michalopoulos, P., Aller, R.C., 2004. Early diagenesis of biogenic silica in the Amazon delta: alteration, authigenic clay formation, and storage. Geochem. Cosmochim. Acta 68 (5), 1061–1085.

Mii, H.-S., Grossman, E.L., Yancey, T.E., Chuvashov, B., Egorov, A., 2001. Isotopic records of brachiopod shells from the Russian Platform — evidence for the onset of mid-Carboniferous glaciation. Chem. Geol. 175 (1), 133–147.

Milucka, J., et al., 2012. Zero-valent sulphur is a key intermediate in marine methane oxidation. Nature 491 (7425), 541–546.

Mitchum, R.M., Van Wagoner, J.C., 1991. High-frequency sequences and their stacking patterns: sequence-stratigraphic evidence of high-frequency eustatic cycles. Sediment. Geol. 70 (2), 131–160.

Moore, T.S., Murray, R.W., Kurtz, A.C., Schrag, D.P., 2004. Anaerobic methane oxidation and the formation of dolomite. Earth Planet. Sci. Lett. 229 (1–2), 141–154.

Moseley, F., 1952. The namurian of the lancaster fells. Q. J. Geol. Soc. 109 (1–4), 423–450 NP,451-454.

Moseley, F., 1962. The structure of the south-western Part Of the sykes anticline, Bowland, west yorkshire. Proc. Yorks. Geol. Polytech. Soc. 33 (3), 287–314.

Mossmann, J.-R., Aplin, A.C., Curtis, C.D., Coleman, M.L., 1991. Geochemistry of inorganic and organic sulphur in organic-rich sediments from the Peru Margin. Geochem. Cosmochim. Acta 55 (12), 3581–3595.

Nesbitt, E.A., Martin, R.A., Campbell, K.A., 2013. New records of Oligocene diffuse hydrocarbon seeps, northern Cascadia margin. Palaeogeogr. Palaeoclimatol. Palaeoecol. 390, 116–129.

Newell, A., Vane, C.H., Sorensen, J., Moss-Hayes, V., D, G., 2016. Long-term Holocene groundwater fluctuations in a chalk catchment: evidence from Rock-Eval pyrolysis of riparian peats. Hydrol. Process. 30, 4556–4567.

Newport, S.M., Jerrett, R.M., Taylor, K.G., Hough, E., Worden, R.H., 2018. Sedimentology and microfacies of a mud-rich slope succession: in the carboniferous Bowland basin, NW England (UK). J. Geol. Soc. 175 (2), 247–262.

Nissenbaum, A., Kaplan, I.R., 1972. Chemical and isotopic evidence for the in situ origin of marine humic substances. Limnol. Oceanogr. 17 (4), 570–582.

Nissenbaum, A., Presley, B.J., Kaplan, I.R., 1972. Early diagenesis in a reducing fjord, Saanich Inlet, British Columbia—I. chemical and isotopic changes in major components of interstitial water. Geochem. Cosmochim. Acta 36 (9), 1007–1027.

Orr, W., 1986. Kerogen/asphaltene/sulfur relationships in sulfur-rich Monterey oils. Adv. Org. Geochem. 10, 499–516.

Passey, Q., Bohacs, K.M., Esch, W., Klimentidis, R., Sinha, S., 2010. From oil-prone source rock to gas-producing shale reservoir - geologic and petrophysical characterisation of unconventional shale-gas reservoirs. In: CPS/SPE International Oil and Gas Conference and Exhibition, Beijing.

Pedersen, M., Nielsen, J.K., Boyce, A.J., Fallick, A.E., 2003. Timing and genesis of base-metal mineralisation in black shales of the upper permian ravnefjeld formation, wegener halvø, east Greenland. Miner. Depos. 38 (1), 108–123.

Peters-Kottig, W., Strauss, H., Kerp, H., 2006. The land plant δ13C record and plant evolution in the Late Palaeozoic. Palaeogeogr. Palaeoclimatol. Palaeoecol. 240 (1–2), 237–252.

Peters, K.E., 1986. Guidelines for evaluating petroleum source rock using programmed pyrolysis. AAPG (Am. Assoc. Pet. Geol.) Bull. 70 (3), 318.

Peters, K.E., Walters, C.C., Moldowan, J., 2005. The Biomarker Guide: Volume 2: Biomarkers and Isotopes in Petroleum Exploration and Earth History. Cambridge University Press, Cambridge.

Pharaoh, T., et al., 2019. The Môn-Deemster-Ribblesdale Fold-Thrust Belt, Central UK: a concealed variscan inversion belt located on weak caledonian crust. Geol. Soc. Lond. Spec. Publ. 490 SP490-2018-109.

Pillot, D., Deville, E., Prinzhofer, A., 2014. Identification and quantification of carbonate species using Rock-Eval pyrolysis. Oil Gas Sci. Technol. Revue d'IFP Energies Nouvelles 69 (2), 341–349.

Pirlet, H., et al., 2010. Diagenetic formation of gypsum and dolomite in a cold-water coral mound in the Porcupine Seabight, off Ireland. Sedimentology 57 (3), 786–805.

Posamentier, H.W., Jervey, M.T., Vail, P.R., 1988. Eustatic Controls on Clastic Deposition I - Conceptual Framework. Society of Economic Paleontologists and Mineralogists Special Publication 42.

Poulton, S.W., Canfield, D.E., 2005. Development of a sequential extraction procedure for iron: implications for iron partitioning in continentally derived particulates. Chem. Geol. 214 (3), 209–221.

Poulton, S.W., Canfield, D.E., 2011. Ferruginous conditions: a dominant feature of the ocean through earth's history. Elements 7 (2), 107–112.

Poulton, S.W., Fralick, P.W., Canfield, D.E., 2004a. The transition to a sulphidic ocean ∼ 1.84 billion years ago. Nature 431, 173.

Poulton, S.W., Krom, M.D., Raiswell, R., 2004b. A revised scheme for the reactivity of iron (oxyhydr)oxide minerals towards dissolved sulfide. Geochem. Cosmochim. Acta 68 (18), 3703–3715.

Poulton, S.W., Raiswell, R., 2002. The low-temperature geochemical cycle of iron: from continental fluxes to marine sediment deposition. Am. J. Sci. 302 (9), 774–805.

Prahl, F.G., Cowie, G.L., De Lange, G.J., Sparrow, M.A., 2003. Selective organic matter preservation in "burn-down" turbidites on the Madeira Abyssal Plain. Paleoceanography 18 (2) n/a-n/a.

Pratt, L.M., Davis, C.L., 1992. Intertwined fates of metals, sulfur, and organic carbon in black shales. In: Pratt, L.M., Comer, J.B., Brassell, S.C., Droppo, R. (Eds.), Geochemistry of Organic Matter in Sediments and Sedimentary Rocks. SEPM Society for Sedimentary Geology.

Raiswell, R., Canfield, D., 1998. Sources of iron for pyrite formation in marine sediments. Am. J. Sci. 298 (3), 219–245.

Ramsbottom, W.H.C., 1973. Transgressions and regressions in the dinantian: a new synthesis of British dinantian stratigraphy. Proc. Yorks. Geol. Polytech. Soc. 39 (4), 567–607.

Ramsbottom, W.H.C., 1977. Major cycles of transgression and regression (mesothems) in the Namurian. Proc. Yorks. Geol. Polytech. Soc. 41 (3), 261–291.

Ramsbottom, W.H.C., Rhys, G.J., Smith, E.G., 1962. Boreholes in the carboniferous rocks of the ashover district, derbyshire. Bull. Geol. Surv. G. B. 19, 75–168.

Ramsbottom, W.H.C., Saunders, W.B., 1985. Evolution and evolutionary biostratigraphy of carboniferous ammonoids. J. Paleontol. 59 (1), 123–139.

Riegel, W., 1996. The geologic significance of the Late Paleozoic phytoplankton blackout. In: IX IPC Meeting, Houston, Texas, USA Abstracts, pp. 133–134.

Riegel, W., 2008. The Late Palaeozoic phytoplankton blackout — artefact or evidence of global change? Rev. Palaeobot. Palynol. 148 (2), 73–90.

Riley, D.A., Pearce, T.J., Mathia, E., Ratcliffe, K., Martin, J., 2016. The application of elemental geochemistry to UK onshore unconventional plays. Geol. Soc. Lond. Pet. Geol. Conf. Ser. 8.

Riley, N., 1988. Stratigraphy of the BP Minerals BH MHD 4. Marl Hill Whitewell, Lancs. BGS Technical Report No. WH/88/300R.

Riley, N., et al., 1993. Geochronometry and Geochemistry of the European Mid-carboniferous Boundary Global Stratotype Proposal, Stonehead Beck, vol. 116. Annales de la Societe geologique de Belgique, T, North Yorkshire, UK, pp. 275–289 fascicule 2.

Rygel, M.C., Fielding, C.R., Frank, T.D., Birgenheier, L.P., 2008. The magnitude of late paleozoic glacioeustatic fluctuations: a synthesis. J. Sediment. Res. 78 (8), 500–511.

Sadler, P., 1999. The Influence of Hiatuses on Sediment Accumulation Rates. GeoResearch Forum.

Sadler, P.M., 1981. Sediment accumulation rates and the completeness of stratigraphic sections. J. Geol. 89 (5), 569–584.

Sadler, P.M., Jerolmack, D.J., 2014. Scaling Laws for Aggradation, Denudation and Progradation Rates: the Case for Time-Scale Invariance at Sediment Sources and Sinks. vol. 404. Geological Society, London, pp. SP404–S407 Special Publications.

Schieber, J., Southard, J., Schimmelmann, A., 2010. Lenticular shale fabrics resulting from intermittent erosion of water-rich muds - interpreting the rock record in the light of recent flume experiments. J. Sediment. Res. 80, 119–128.

Scotchman, I.C., 1989. Diagenesis of the kimmeridge clay formation, onshore UK. J. Geol. Soc. 146 (2), 285–303.

Sholkovitz, E.R., Price, N.B., 1980. The major-element chemistry of suspended matter in the Amazon Estuary. Geochem. Cosmochim. Acta 44 (2), 163–171.

Sinninghe Damsté, J.S., Rijpstra, W.I.C., Leeuw, J.W.d., Schenck, P.A., 1987. Origin of organic sulphur compounds and sulphur-containing high molecular weight substances in sediments and immature crude oils. Adv. Org. Geochem. 13 (4–6).

Soetaert, K., Hofmann, A.F., Middelburg, J.J., Meysman, F.J.R., Greenwood, J., 2007. The effect of biogeochemical processes on pH. Mar. Chem. 105 (1), 30–51.

Spears, D.A., Amin, M.A., 1981. Geochemistry and mineralogy of marine and non-marine Namurian black shales from the Tansley Borehole, Derbyshire. Sedimentology 28 (3), 407–417.

Stephenson, M.H., et al., 2010. Northern England Serpukhovian (early Namurian) farfield responses to southern hemisphere glaciation. J. Geol. Soc. 167 (6), 1171–1184.

Stephenson, M.H., Millward, D., Leng, M.J., Vane, C.H., 2008. Palaeoecological and possible evolutionary effects of early Namurian (Serpukhovian, Carboniferous) glacioeustatic cyclicity. J. Geol. Soc. 165 (6), 993–1005.

Sun, M.-Y.i., Aller, R.C., Lee, C., Wakeham, S.G., 2002. Effects of oxygen and redox oscillation on degradation of cell-associated lipids in surficial marine sediments. Geochem. Cosmochim. Acta 66 (11), 2003–2012.

Tappan, H., 1970. Phytoplankton abundance and Late Paleozoic extinctions: a reply. Palaeogeogr. Palaeoclimatol. Palaeoecol. 8 (1), 56–66.

Taylor, S., McLennan, S., 1985. The Continental Crust: its Composition and Evolution. Blackwell Scientific, London, pp. 312.

Tegelaar, E.W., de Leeuw, J.W., Derenne, S., Largeau, C., 1989. A reappraisal of kerogen formation. Geochem. Cosmochim. Acta 53 (11), 3103–3106.

Thamdrup, B., 2000. Bacterial manganese and iron reduction in aquatic sediments. In: Schink, B. (Ed.), Advances in Microbial Ecology. Springer US, Boston, MA, pp. 41–84.

Tissot, B., Pelet, R., 1981. Sources and Fate of Organic Matter in Ocean Sediments. Oceanologica Acta Special issue.

Tissot, B., Welte, D., 1984. Petroleum Formation and Occurrence. Springer-Verlag.

Tong, H., Chen, D., 2012. First discovery and characterizations of late Cretaceous seep carbonates from Xigaze in Tibet, China. Chin. Sci. Bull. 57 (33), 4363–4372.

Tribovillard, N., Algeo, T., Lyons, T., Ruboulleau, A., 2006. Trace metals as paleoredox and paleoproductivity proxies: an update. Chem. Geol. 232, 12–32.

Tribovillard, N., Algeo, T.J., Baudin, F., Riboulleau, A., 2012. Analysis of marine environmental conditions based on molybdenum–uranium covariation—applications to Mesozoic paleoceanography. Chem. Geol. 324–325, 46–58.

Tribovillard, N., Bialkowski, A., Tyson, R.V., Lallier-Vergès, E., Deconinck, J.F., 2001. Organic facies variation in the late Kimmeridgian of the Boulonnais area (northernmost France). Mar. Pet. Geol. 18 (3), 371–389.

Tyson, R.V., Pearson, T.H., 1991. Modern and ancient continental shelf anoxia: an overview. Geol. Soc. Lond. Spec. Publ. 58 (1), 1–24.

Veevers, J.J., Powell, C.M., 1987. Late Paleozoic glacial episodes in Gondwanaland reflected in transgressive-regressive depositional sequences in Euramerica. Geol. Soc. Am. Bull. 98 (4), 475–487.

Warr, L.N., 2000. The variscan orogeny: the welding of pangaea. In: Woodcock, N.H., Strachan, R. (Eds.), Geological History of Britain and Ireland. Wiley-Blackwell, Hoboken, USA, pp. 271–294.

Waters, C.N., Browne, M.A.E., Dean, M.T., Powell, J.H., 2007. Lithostratigraphical Framework for Carboniferous Successions of Great Britain (Onshore). British Geological Survey Research Report RR/07/01.

Waters, C.N., Condon, D.J., 2012. Nature and timing of late mississippian to mid-pennsylvanian glacio-eustatic sea-level changes of the pennine basin, UK. J. Geol. Soc. 169 (1), 37–51.

Waters, C.N., Davies, S.J., 2006. Carboniferous: extensional basins, advancing deltas and coal swamps. In: Brenchley, P.J. (Ed.), The Geology of England and Wales. Geological Society of London, London, England, pp. 173–223.

Waters, C.N., Millward, D., Thomas, C.W., 2014. The Millstone Grit group (pennsylvanian) of the northumberland–solway basin and alston block of northern England. Proc. Yorks. Geol. Soc. 60 (1), 29–51.

Waters, C.N., et al., 2019. Lithological and chemostratigraphic discrimination of facies within the Bowland Shale Formation within the craven and edale basins, UK. Pet. Geosci. https://doi.org/10.1144/petgeo2018-039.

Waters, C.N., Waters, R.A., Barclay, W.J., Davies, J.R., 2009. A Lithostratigraphical Framework for the Carboniferous Successions of Southern Great Britain (Onshore). British Geological Survey Research Report RR/09/01.

Wei, W., Algeo, T.J., 2019. Elemental proxies for paleosalinity analysis of ancient shales and mudrocks. Geochem. Cosmochim. Acta. https://doi.org/10.1016/j.gca.2019.06.034.

Yurchenko, A.Y., 2014. The genesis of calcite in carbonate rocks of the sedimentary basins: evidence from the stable carbon and oxygen isotopes composition. Mosc. Univ. Geol. Bull. 69 (5), 375–378.